Ocean Engineering 343 (2026) 123379

Contents lists available at ScienceDirect

Ocean Engineering

journal homepage: www.elsevier.com/locate/oceaneng

Research paper

Real-time damage detection and localization in ship structures using iFEM and machine learning techniques

Jacopo Bardiani [a,*], Roberto Faure Ragani [a], Andrea Manes [a], Claudio Sbarufatti [a], Adnan Kefal [b]

[a] Department of Mechanical Engineering, Politecnico di Milano, Via G. La Masa 1, 20156 Milano, Italy
[b] Faculty of Engineering and Natural Sciences, Sabanci University, Tuzla, Istanbul, 34956, Turkey

ARTICLE INFO

Keywords:
Inverse finite element method
Anomaly index
Ship structures
Machine learning
Extreme environmental conditions
Structur al health monitoring

ABSTRACT

This paper presents an advancement in smart sensing and structural health monitoring (SHM) of large-scale ship structures, aimed at real-time detection and accurate localization of damage induced by extreme environmental conditions and high-impact events. This subject has attracted increasing attention in naval architecture, marine, and ocean engineering because such damage has critical implications for structural integrity and safety. In practical applications within harsh marine environments, the capability to rapidly and reliably identify the location of structural damage after an extreme event is essential. To address this need, the proposed approach integrates the inverse finite element method (iFEM), anomaly index formulation, and machine learning (ML) techniques. High-fidelity finite element (FEM) models are employed to simulate damage scenarios with high accuracy; these simulations are then simplified to enable efficient real-time analysis and seamless integration into the SHM framework. The methodology has been applied to a representative case study involving a portion of a containership, effectively overcoming challenges related to optimal sensor placement, environmental variability, and complex operating conditions. Ultimately, the study introduces an enhanced iFEM-based strategy combined with ML models for real-time SHM, providing a robust and scalable solution for damage detection and localization in large-scale ship structures under extreme conditions.

1. Introduction

The structural integrity and damage assessments of ships and marine vessels, both civilian and research-oriented, are critical for ensuring their operational safety and effectiveness, particularly when subjected to high-impact events or shock wave loads from accidental collisions, underwater seismic activities, or extreme environmental conditions. As marine technologies continue to advance and vessels operate in increasingly demanding environments, it is vital to accurately assess the extent of structural damage and the ships' condition to determine appropriate actions for restoring functionality and ensuring continued operability. In recent years, emerging maritime challenges, such as debris impact from offshore activities and high-energy wave events, have highlighted the need for real-time structural monitoring to avoid catastrophic consequences and ensure crew safety through timely decision-making (Bursuc et al., 2024; Pettyjohn et al., 2024).

Traditional non-destructive testing methods, such as visual inspection, liquid penetrant, radiography, and magnetic particle testing, are not feasible in emergency situations during a mission, where significant damage such as hull breaches can occur and where the speed of the assessment is crucial (Kroworz and Katunin, 2018; Oboe et al., 2023). In such an extreme context, rapid detection and assessment of hull damage through Structural Health Monitoring (SHM) can be critical in preventing catastrophic consequences, ensuring that necessary actions are taken quickly to mitigate the impact and maintain the integrity of the vessel (i.e. recoverability) (Kefal et al., 2016). The main challenge of any SHM system is to inversely infer structural health from in-situ sensor data, possibly in real-time (Silva-Campillo et al., 2023), capitalizing on the advancements in new sensors, wireless communication networks, and big data analytics coupled with machine learning (ML) techniques (Sbarufatti et al., 2014).

Two main approaches are available to solve SHM inverse tasks: data-driven and model-based. Data-driven algorithms use experimental data collected from sensors and applies statistical or ML techniques to

* Corresponding author. Department of Mechanical Engineering, Politecnico di Milano, Via G. La Masa 1, Italy.
E-mail address: jacopo.bardiani@polimi.it (J. Bardiani).

https://doi.org/10.1016/j.oceaneng.2025.123379
Received 3 June 2025; Received in revised form 5 October 2025; Accepted 29 October 2025
Available online 8 November 2025

identify patterns and diagnose damages (Deraemaeker et al., 2008). Model-based algorithms, on the other hand, rely on physical or mathematical models to predict the behavior of a structure analyzing deviations between the model's predictions and actual data, indicating potential anomalies like damages. Given the high complexity of the ship hull structures and due to difficulties in retrieval of experimental data, model-based approaches appeared as a more suitable and cost-effective choice (Gardner, 2018), especially when multiple levels of the diagnostic hierarchical structure are inferred (Rytter et al., 1993), requiring examples for pattern recognition.

However, one main challenge in ship hull monitoring is the definition of diagnostic techniques that can deal with varying (and often unknown) boundary load conditions, which hamper their applicability in real scenarios if not correctly considered (Sbarufatti et al., 2013). For example, while radar exists to identify the sea state, the pressure distribution along the ship hull surfaces will remain unknown, though necessary for displacement and strain full-field reconstruction. To handle this issue, the inverse Finite Element Method (iFEM) is proposed in the literature as a model-based approach for calculating structural displacements (often referred to as shape sensing or deflection monitoring) based on a set of strain measurements as the sole input (Tessler and Spangler, 2003), typically relying on fiber optic sensor technology or conventional strain gauges/rosettes. The iFEM models only require a mesh discretization of the structure and the definition of structural boundary conditions, without any dependence on the applied external load if a proper sensor network is designed to capture the significant load paths. The iFEM approach consists of minimizing (in a least-squares framework) a weighted error functional defined as the difference between measured and numerically formulated strains. The procedure is computationally efficient, involving mainly matrix-vector multiplications, and fast enough for real-time implementation both in static and dynamic applications (Tessler and Spangler, 2005).

Since its inception, the iFEM algorithm has undergone significant advancements and has been applied to a wide array of shape sensing and structural health monitoring problems. This innovative methodology has been extended to various structural types, such as aerospace plate/beam-like structural components (Oboe et al., 2021a; Papa et al., 2017; Esposito et al., 2023; Kefal et al., 2022), ship structures, e.g., container ships (Kefal & Oterkus, 2016a), bulk carriers (Kefal et al., 2018), and chemical tankers (Kefal and Oterkus, 2016), long underwater pipelines (Zhu et al., 2022a, 2022b), and offshore structures (Li et al., 2020). Moreover, iFEM has found applications in critical areas like pitting corrosion (due to marine environment) identification (Ghasemzadeh et al., 2023), complex load reconstruction (Colombo et al., 2019, 2021; Esposito, 2024), modal shape identification (Belur et al., 2025), showcasing its versatility and robustness.

Further, numerous inverse element formulations have been introduced in the literature, encompassing elements ranging from beams to shells. Among these, several key inverse-shell elements stand out due to their practicality and accuracy. These include the iMIN3 (Tessler & Spangler, 2004; Tessler and Spangler, 2024), iQS4 (Kefal et al., 2016), and iCS8 (Kefal, 2019) inverse-shell elements, all of which employ C0-continuous interpolation functions based on the first-order shear deformation theory. In particular, the iQS4 element has garnered significant attention for shape sensing applications in both simple and complex geometries. It has been applied to ship and offshore structures as well as stiffened aerospace panels due to its advantages in modeling large-scale structures with low-cost sensor networks and its ability to provide highly accurate displacement estimations (Oboe et al., 2021b; Roy et al., 2020). The iQS4 approach has demonstrated superior performance in damage identification for both monolithic and stiffened structures composed of isotropic or orthotropic materials (Colombo et al., 2019; Abdollahzadeh et al., 2020).

In addition to shell elements, a variety of inverse-beam elements have been developed to facilitate displacement monitoring in thick and thin beam structures. Experimental and numerical investigations have consistently highlighted their high efficiency and accuracy for real-time deformation detection (Gherlone et al., 2012, 2014). Notably, fiber Bragg grating (FBG) sensors have been employed for dynamic displacement prediction of beam structures, further validating the applicability of iFEM in real-world scenarios (Song and Liang, 2018). More recently, the integration of isogeometric analysis into iFEM has led to the development of the isogeometric iFEM approach. This method leverages non-uniform rational B-splines (NURBS) for the discretization of both structural geometry and displacement fields, thereby enhancing the precision and smoothness of the reconstructed deformations (Kefal and Oterkus, 2020). Further advancements in iFEM have included the incorporation of refined displacement theories, such as the refined zigzag theory (RZT) (Tessler et al., 2010). This combination (Cerracchio et al., 2015; Kefal et al., 2017) enables the reconstruction of zigzag deformations across the thickness of sandwich plates, shells, and beams. Numerical and experimental studies have validated the predictive capabilities of the iFEM-RZT method, particularly for moderately thick, wing-shaped sandwich panels (Zhao et al., 2021; Kefal et al., 2021a; Poloni et al., 2023a, 2023b).

The continuous evolution of iFEM through novel mathematical formulations, combined experimental and numerical validations, and integration with advanced theories and computational methods underscores its potential as a critical tool in modern structural engineering. Its adaptability across various structural configurations and materials, coupled with its proven effectiveness in real-time monitoring, positions iFEM as a leading methodology for next-generation SHM solutions. However, in practical applications, the iFEM method faces certain limitations due to the inability to place sensors uniformly across the entire structure. Sensor deployment is often restricted by hardware limitations and accessibility constraints, meaning that only certain areas of the structure can be sensorized (Kefal et al., 2016; Oboe et al., 2022), affecting the overall accuracy of the displacement reconstruction. To mitigate this issue, pre-extrapolation techniques are employed, allowing for the estimation of strain data in areas without sensor coverage (Oboe et al., 2023). These techniques can be based on physical laws (Oboe et al., 2022) or on data-driven approaches, like the smoothing element analysis (SEA) (Kefal et al., 2021; Roy et al., 2022) or simpler polynomial functions, as implemented in this study. Further, another novel pre-extrapolation strategy based on Modal Virtual Sensor Expansion is proposed in (Esposito, 2024). Particularly, the "smoothed iFEM" formulation (Kefal et al., 2021b) is a two-step approach that involves generating smooth, continuous strain data from discrete sensor measurements, which is then used for shape sensing via the classical iFEM framework. Comparative studies have shown that smoothed iFEM offers improved accuracy over traditional formulations, making it highly effective for real-time applications.

In addition to displacement reconstruction, iFEM has also been effectively used as a tool for damage identification, exploiting a set of test sensors to reveal damage sensitive features. This is done in (Colombo et al., 2019) by considering a healthy mesh for the iFEM, which will reconstruct a strain field always compatible with the healthy structure; if a non-modelled geometrical modification (e.g. due to damage) induces a strain field perturbation as input to the test sensors, the iFEM (based on a healthy mesh) will reconstruct a displacement field not compatible with the real strain observation. Various methods have been implemented in the literature to synthesize and measure this non compatibility, e.g. leveraging the Von Mises strain (Li et al., 2020) for the definition of load-independent damage indices (Colombo et al., 2019). Further research aimed at damage detection with iFEM is presented in (Roy et al., 2021; Roy and Gherlone, 2023). More recently, iFEM has been integrated with peridynamics (PD) (Silling et al., 2010) to enable simultaneous shape sensing and crack propagation monitoring. This integration opens new avenues for non-local damage detection and monitoring, further broadening the scope of iFEM applications in SHM (Kefal et al., 2023). Most recently, the damage/crack propagation aimed to be monitored by using just sensor data, through the invocative

development of particle inverse method (Kefal et al., 2024), which is essentially originated based on the idea of iFEM's least squares formulations.

Several contributions have specifically combined iFEM with anomaly index formulations for damage detection. Colombo et al. (2019, 2021) investigated the use of iFEM-based anomaly indices on composite and metallic plates with artificial cracks and cut-outs, showing that discrepancies between reconstructed and measured strains could serve as reliable indicators of localized damage. Oboe et al. (2023) extended this approach to stiffened aerospace-type panels, validating the method experimentally and confirming its robustness in laboratory-scale conditions. More recently, Bardiani et al. (2024) applied the anomaly index strategy to naval-type plate structures subjected to localized damage, demonstrating its feasibility through numerical simulations but still within simplified structural layouts. In parallel, the integration of iFEM with machine learning (ML) has been explored in only a few studies: Li et al. (2022), for example, employed artificial neural networks to process iFEM-derived strain features for crack detection in aerospace panels, highlighting the potential of data-driven models to complement iFEM but without addressing large marine structures or extreme loading scenarios. To the best of our knowledge, no published research has yet employed ML to overcome the intrinsic limitations of the anomaly index in naval applications, namely the reliance on dense sensor networks and the difficulty of capturing complex or distributed damage morphologies induced by extreme loads. These limitations are consistent with what has already been observed in previous anomaly index formulations, namely their restriction to simple and small-scale damage cases and their dependence on many test sensors.

The main and novel aim of this study is to propose an improved framework based on the iFEM with polynomial pre-extrapolation and integrating ML algorithms for localizing complex damage in large and intricate structures, such as ships and marine vessels. Ultimately, this paper presents for the first time seamless integration of iFEM, anomaly index formulation (Colombo et al., 2021), and deep neural networks (DNNs) specifically tailored for damage identification and localization of any real ship structures. By leveraging advanced computational models, this improved approach seeks to significantly enhance the applicability and effectiveness of real-time monitoring by iFEM in real-world, large-scale structures. This enhancement not only aims to improve the accuracy of damage assessments but also allows us to facilitate timely decision-making in critical situations, ultimately contributing to the operational safety and integrity of various engineering applications. This is particularly relevant in cases where the damage exhibits a non-trivial morphology, as often observed in high-impact scenarios involving accidental blast events, collisions, debris strikes, or extreme wave events. In the novel framework, complex damage configurations are initially simulated using high-fidelity computational models and subsequently simplified (Lloyd's Register, 2019), ensuring that the reduced models still capture the key structural responses. Additionally, an ML approach based on DNNs is employed to predict damage location using a reduced set of Anomaly Indexes (Colombo et al., 2019), derived from a limited number of strategically placed rosette sensors. The ML model is trained using simplified damage cases but demonstrates the ability to generalize to more realistic, high-fidelity scenarios. The proposed method is implemented in a representative application of a portion of a containership, addressing challenges such as limited sensor deployment, harsh environmental conditions, and operational constraints—all of which complicate accurate damage diagnosis in real-world maritime structures.

The manuscript is organized as follows: Section 2 reviews the iFEM methodology, the anomaly index formulation, and the coupling with the machine learning model. Section 3 describes the case study, including the high-fidelity impact model, damage simulation, iFEM reconstruction, and DNNs for damage localization, along with the evaluation of generalization capability and results. Section 4 concludes the study.

2. The iFEM/iQS4 review and its methodological coupling with machine learning methods

2.1. Formulation of the iFEM/iQS4 element

A summary of the iFEM approach for displacement and strain field reconstruction is provided in this section, while a detailed formulation is available in (Kefal et al., 2016b; Kefal and Oterkus, 2016; Oboe et al., 2023) for the interested reader.

In this study, a generic shell structure — such as a panel of a ship hull — is discretized using inverse elements, with the iQS4 formulation being specifically adopted (Kefal et al., 2016) (Fig. 1). The displacement field is calculated starting from input strain measurements by minimizing the least-square functional of Equation (1), which is defined as the error between the input strain field measured by sensors $(\cdot)^{\varepsilon}$ and its numerical formulation $(\cdot)(\boldsymbol{u})$, which is a function of the unknown nodal displacements $\boldsymbol{u}$. Both the input and numerical strain fields are separated into three main components: the membrane $\boldsymbol{e}$, the bending $\boldsymbol{k}$, and the transverse shear $\boldsymbol{g}$ strain contributions. Thus, the formulation of the *i-th* inverse element can be defined as:

$$\Phi_i(\boldsymbol{u}^i) = \left\|\boldsymbol{e}(\boldsymbol{u}^i) - \boldsymbol{e}_i^{\varepsilon}\right\|^2_{\boldsymbol{W}_m^i} + \left\|\boldsymbol{k}(\boldsymbol{u}^i) - \boldsymbol{k}_i^{\varepsilon}\right\|^2_{\boldsymbol{W}_b^i} + \left\|\boldsymbol{g}(\boldsymbol{u}^i) - \boldsymbol{g}_i^{\varepsilon}\right\|^2_{\boldsymbol{W}_s^i} \tag{1}$$

Where $\|\cdot\|^2_{\boldsymbol{W}}$ is the squared weighted Euclidean norm with the weight matrix $\boldsymbol{W}$. Specifically, $\boldsymbol{W}_m^i$, $\boldsymbol{W}_b^i$, and $\boldsymbol{W}_s^i$ are diagonal matrices of weights for the membrane, bending, and transverse shear strain contributions, respectively (Oboe et al., 2023). Generally, a unitary reference value is assigned to elements where the input strain field component is measured by physical sensors ($\boldsymbol{e}_i^{\varepsilon}$, $\boldsymbol{k}_i^{\varepsilon}$ and $\boldsymbol{g}_i^{\varepsilon}$), while in other cases (missing in-situ strain component), the coefficients are reduced to small values (e.g., 10^{-4}).

In the broadest scenario, the input strain formulation is derived from strain measurements taken on the structure. Sensors are typically placed on the external surfaces of the component for easier installation and maintenance, although applications with embedded sensors are also feasible.

For example, consider a couple of strain gauge rosettes applied on the two external sides of the shell as shown in Fig. 1. The membrane and the bending strain components associated with the *j-th* sensors' location within the *i-th* inverse element can be defined as:

$$\boldsymbol{e}_{ij}^{\varepsilon} = \frac{1}{2}\begin{Bmatrix} \varepsilon_{xx}^{+} + \varepsilon_{xx}^{-} \\ \varepsilon_{yy}^{+} + \varepsilon_{yy}^{-} \\ \gamma_{xy}^{+} + \gamma_{xy}^{-} \end{Bmatrix}_j \quad \boldsymbol{k}_{ij}^{\varepsilon} = \frac{1}{2h}\begin{Bmatrix} \varepsilon_{xx}^{+} - \varepsilon_{xx}^{-} \\ \varepsilon_{yy}^{+} - \varepsilon_{yy}^{-} \\ \gamma_{xy}^{+} - \gamma_{xy}^{-} \end{Bmatrix}_j \tag{2}$$

Where $2h$ is the shell thickness at the sensors' location.

The strain component $\boldsymbol{g}$, on the other hand, cannot be directly computed from the measured surface strain components. However, since its contribution can be neglected in most engineering applications, the experimental input component of $\boldsymbol{g}$ is supposed to be null (Kefal et al., 2016).

For precise reconstruction of the displacement field, it is necessary to have the input strain field available for all elements of the structure. However, this is generally impractical in real-world applications. To address this limitation, strains can be extrapolated in areas where physical sensors are unavailable. This can be achieved through methods such as polynomial fitting or Smoothing Element Analysis (SEA) (Kefal et al., 2021; Poloni et al., 2023a, 2023b), utilizing either data-driven or physics-based approaches. Data-driven methods extrapolate strains solely based on the acquired strain field, resulting in a more continuous and smooth output across the entire domain. Conversely, physics-based strain extrapolation combines the acquired strain data with knowledge of geometrical discontinuities and their analytical formulations to provide a more accurate strain field, especially in the presence of discontinuities (Bardiani et al., 2024, 2025a).

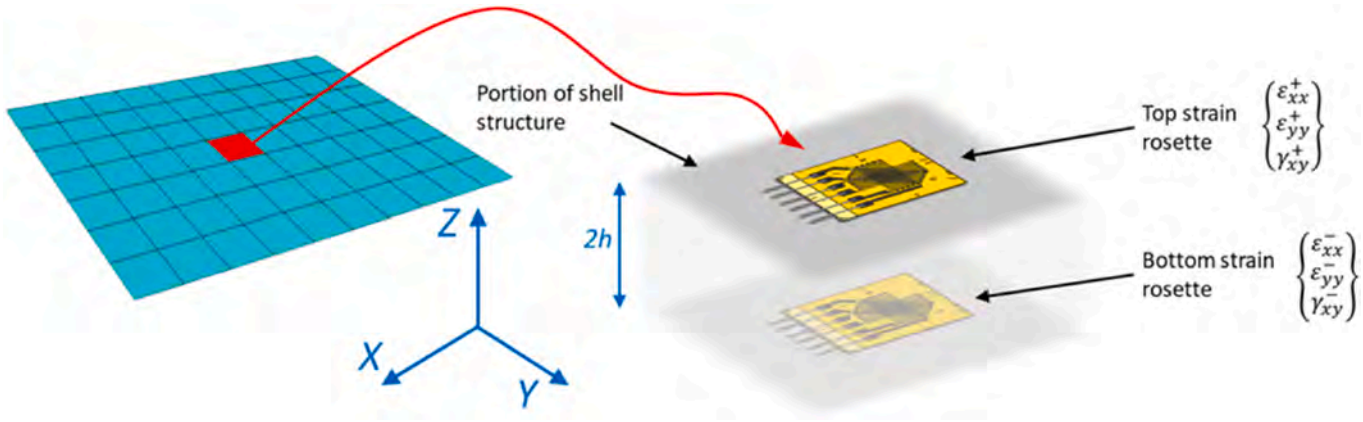

Fig. 1. Discrete sensor placement on both the top and bottom surfaces of the shell structure (adapted with permission from (Oboe et al., 2023)).

The numerical strain components formulation is based on the element's shape functions, thus, it is computed through Eq. (3), where $\boldsymbol{B}^m$, $\boldsymbol{B}^b$, and $\boldsymbol{B}^s$ are matrices containing the derivative of the shape functions (Kefal et al., 2016).

$$\boldsymbol{e}(\boldsymbol{u}^i) = \boldsymbol{B}^m \boldsymbol{u}^i \; \boldsymbol{k}(\boldsymbol{u}^i) = \boldsymbol{B}^b \boldsymbol{u}^i \; \boldsymbol{g}(\boldsymbol{u}^i) = \boldsymbol{B}^s \boldsymbol{u}^i \tag{3}$$

After some mathematical passages applied to Eqs. (2) and (3) inside Eq. (1), by employing a conventional assembly procedure that accounts for the contribution of each inverse element and aims to minimize the global least-squared functional, the problem can be formulated as follows:

$$\boldsymbol{K}\boldsymbol{U} = \boldsymbol{F} \tag{4}$$

Where $\boldsymbol{K}$ is a matrix resembling the stiffness linking the global displacement field $\boldsymbol{U}$ with the vector $\boldsymbol{F}$ containing the input strain field contribution.

Nonetheless, the matrix $\boldsymbol{K}$ is singular and, if left unconstrained, it will result in a rigid motion of the structure. Therefore, after establishing appropriate boundary conditions, the free (unconstrained) nodal displacements can be determined. Subsequently, once the displacements field has been calculated, the numerical strain field $\boldsymbol{\varepsilon}^{iFEM}$ can be computed using Eq. (3), similarly to any direct FEM approach.

2.2. Anomaly index formulation for iFEM-based damage identification

The iFEM strategy can be used for damage identification (Colombo et al., 2019, 2021). The basic assumption is that the presence of a defect modifies the strain field of a structure with respect to its healthy condition. If a numerical model is constrained to reproduce the behaviour of a defect-free structure, any incompatibility between the reconstructed field and the actual measured strains can be interpreted as an indication of damage. To this end, the methodology introduces a load-independent anomaly index, denoted as $i(x_t)$, which quantifies the deviation between the strain field reconstructed by iFEM and the one experimentally measured at specific locations. A fundamental point of this approach is the distinction between two different sensor networks: the input sensor network and the test sensor network.

- The input sensors ($\boldsymbol{\varepsilon}_{in}$), placed at locations $\boldsymbol{x}_{in}$, provide the strain data that are directly supplied to the iFEM procedure. Based on these values, the iFEM algorithm reconstructs the displacement and strain fields over the entire discretized geometry of the structure. Since the underlying iFEM mesh represents the healthy structure (i.e., the iFEM model does not have any prior knowledge about whether the structure is damaged or not), the reconstructed strain field $\boldsymbol{\varepsilon}_{iFEM}$ is always kinematically compatible with the assumed undamaged geometry. In practice, this means that even if the actual component is damaged, the iFEM reconstruction will "force" the strain field into a form that is admissible for a healthy structure, thus hiding the local perturbations introduced by the defect.
- The test sensors ($\boldsymbol{\varepsilon}_t$), located at positions $\boldsymbol{x}_t$, are not involved in the iFEM reconstruction. Instead, they provide an independent dataset that serves as a benchmark against which the iFEM predictions can be validated. When the structure is intact, the reconstructed strains $\boldsymbol{\varepsilon}_{iFEM}(\boldsymbol{x}_t)$ are expected to match the measured strains $\boldsymbol{\varepsilon}_t(\boldsymbol{x}_t)$, leading to negligible discrepancies. Conversely, when damage occurs, the measured strain field deviates from the reconstructed one, because the iFEM cannot reproduce the local incompatibilities associated with cracks, perforations, or plastification. The comparison between the reconstructed and measured values at the test sensor locations thus provides a robust, load-independent indicator of the presence and location of damage.

This concept is formalized through the anomaly index, defined as (Colombo et al., 2019, 2021):

$$i(x_t) = \frac{\varepsilon_{eq,t}(x_t) - \varepsilon_{eq,iFEM}(x_t)}{\varepsilon_{eq,t}(x_t)} \cdot 100 \tag{5}$$

Where $\varepsilon_{eq,t}(x_t)$ is the equivalent strain measured at the test location and $\varepsilon_{eq,iFEM}(x_t)$ is the equivalent strain reconstructed by iFEM at the same point. The equivalent strain is introduced in Eq. (5) to condense the tensorial strain components into a single scalar, which is frame-invariant and independent of the sensor orientation. In the case of in-plane strain measurements, which are typically available through strain rosettes, the equivalent strain can be computed as:

$$\varepsilon_{eq} = \frac{1}{\sqrt{2}} \cdot \sqrt{(\varepsilon_{xx} - \varepsilon_{yy})^2 + (\varepsilon_{xx})^2 + (\varepsilon_{yy})^2 + 6\gamma_{xy}^2} \tag{6}$$

This expression is particularly suited for practical SHM applications, since strain rosettes provide direct access to the in-plane components ε_{xx}, ε_{yy} and γ_{xy}. Eq. (5) is evaluated independently at each test sensor location x_t, so that every sensor provides a local value of the anomaly index. The collection of all these values forms the anomaly index vector $\boldsymbol{i}(x_t)$, which highlights the presence of damage through non-zero components concentrated near the defective region.

Further details on the theoretical assumptions underlying this formulation can be found in Colombo et al. (2019).

The main properties of the anomaly index are worth emphasizing. First, it reduces the tensorial quantity to a scalar, making it easier to interpret and visualize. Second, it is independent of the coordinate system of the sensors, ensuring robustness with respect to sensor placement. Third, and most importantly, it is independent of the magnitude of the applied load: whether the structure is subjected to small operational loads or to extreme impact events, the index reflects

only the incompatibility due to damage and not the absolute strain level.

When the structure is in a healthy condition, the anomaly index vector $\boldsymbol{i}(x_t)$ is expected to be close to zero at all test sensor locations. This means that the iFEM-reconstructed strains are consistent with the actual measurements, confirming the absence of defects. On the other hand, when damage is present, some components of $i(x_t)$ deviate significantly from zero, especially at test sensors located near the damaged region. In this case, the index reveals the local incompatibility between the measured strain field and the displacement field reconstructed under the assumption of a healthy model.

The entire procedure is illustrated in Fig. 2. Panel (a) summarizes the workflow, which is repeated at each time instant, while panel (b) shows an example of the placement of input and test sensors on a structural component subjected to time-dependent loading. The rationale for employing two distinct sensor networks becomes clear: input sensors are indispensable for enabling the iFEM to reconstruct a global strain field, while test sensors act as an external verification tool, enabling damage detection by highlighting incompatibilities. If only one sensor network were used, iFEM would always perfectly reproduce the input measurements, and any local damage effects would be masked. By maintaining this separation, the proposed strategy ensures both consistent reconstruction and a reliable means of identifying structural anomalies.

It is worth noting that no universal rule exists for determining the optimal locations of the test sensors. Their placement must be carefully defined on a case-by-case basis, considering the geometry of the structure, the type and location of expected damage, boundary conditions, and economic or practical constraints such as accessibility and installation costs. Consequently, the effectiveness of the anomaly index strongly depends on a well-conceived sensor layout, which should balance accuracy, robustness, and feasibility.

As highlighted in the Introduction, the previously developed anomaly index procedure—although successfully applied in both numerical and experimental contexts (Colombo et al., 2019, 2021; Oboe et al., 2023; Bardiani et al., 2024)—still suffers from intrinsic limitations that prevent its straightforward application to realistic large-scale systems. First, it has so far been demonstrated only on laboratory-scale specimens or structural components of limited extension, whereas its applicability to full-size naval or offshore structures remains untested. Second, it has only been verified in the presence of simple and localized damage patterns, such as cracks or delaminations, while its robustness in scenarios involving complex, multiple, or distributed damages has not been assessed. Finally, the method critically relies on a dense network of test sensors to ensure accurate localization, a requirement that becomes technically and economically impractical in large marine structures, where installation and accessibility constraints limit the number of deployable sensors. All these aspects further restrict the scalability of the approach and hinder its integration into digital twin frameworks. These shortcomings emphasize the need for methodological advancement capable of reducing sensor dependency, extending applicability to complex damage scenarios, and ensuring feasibility for large-scale SHM applications in the marine and offshore fields.

To overcome these limitations, two machine learning models based on DNNs are introduced, whose rationale and implementation will be described in detail in the following subsection, before presenting their integration with the iFEM and anomaly index framework.

2.3. Data-driven approach based on DNNs

Neural networks (NNs) are models commonly employed to approximate linear and/or non-linear functions of the form $\boldsymbol{y} = f(\boldsymbol{x})$ between input ($\boldsymbol{x}$) and output ($\boldsymbol{y}$) vectors. NNs consist of interconnected units known as neurons (or nodes), organized into multiple layers: an input layer, one or more hidden layers and an output layer. NNs that contain more than one hidden layer are referred to as DNNs. This machine learning technique is inspired by the learning mechanisms of the human brain, advanced by Hinton et al. (Hinton et al., 2006; Guo et al., 2021; Zhou, 2021). Typically, neurons in consecutive layers are fully connected, meaning that each node in a layer is linked to all the nodes in the subsequent layer. In recent years, they have gained widespread use across various domains of engineering and applied sciences, especially when conventional models struggle to generalize from limited or non-linearly separable data.

The *i-th* component x_i of the input vector ($\boldsymbol{x}$) is assigned to the *i-th* neuron within the input layer, which transfers information to neuron *j* in the subsequent layer through a weighted connection characterized by weight w_{ij}. The information obtained by the *j-th* node is then aggregated

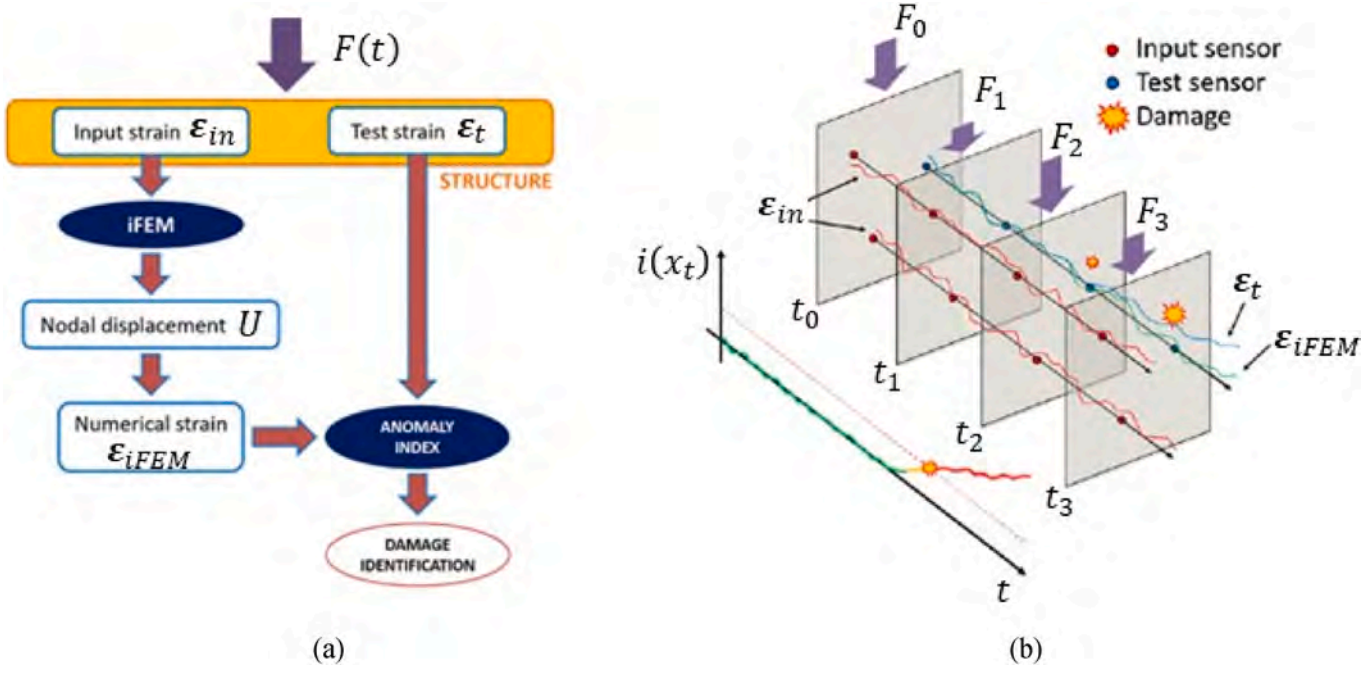

Fig. 2. Anomaly Index evaluation: (a) Workflow followed at each time; (b) Example of input and test sensor placements on a structure experiencing time-dependent loading. Adapted with permission from (Colombo et al., 2021).

and updated according to the following Eq. (11) (Bardiani et al., 2025b):

$$z_j = g\left(\sum_{i=1}^{N_j}(w_{ij}\cdot x_i) + b_j\right) \tag{7}$$

Where z_j is the output of the *j-th* node, $g(\cdot)$ is typically a non-linear activation function, N_j represents the number of nodes from which the *j-th* node receives information, and b_j is a bias parameter. This message passing and aggregation process recurs layer-by-layer until the output layer, where the value of the *k-th* node corresponds to the *k-th* component ($\hat{y}_k$) of the estimated output vector ($\hat{\boldsymbol{y}}$). Weights w_{ij} and biases b_j are trainable parameters of the NN and are optimized during training through error back-propagation algorithms with gradient descent, aimed at minimizing the discrepancy between the expected output ($\boldsymbol{y}$) and the predicted output ($\hat{\boldsymbol{y}}$).

The training set is used to make the NN learn the relationship between inputs and outputs, the validation set serves as a tool to indicate underfitting or overfitting (Zhou, 2021), while the testing set is used after training for evaluating the NN generalization capabilities on unseen data. Across epochs, a user-defined error metric comparing predicted and expected outputs guides the iterative update of trainable parameters using gradient descent, culminating in achieving satisfactory reconstruction error (Hinton et al., 2006).

In the present study, two DNNs are employed with the specific aim of learning the relationship between the anomaly index values—computed at a limited number of test sensor locations on the ship structure—and the corresponding damage position (*X* and *Y* coordinates of the damage centroid). By doing so, the approach alleviates the dependency on a dense network of sensors, while still ensuring accurate localization capabilities. This strategy makes the methodology scalable and applicable to large-scale and complex structural configurations, such as those encountered in naval and offshore engineering.

The choice of using DNNs is motivated by preliminary investigations that showed the inadequacy of more traditional ML approaches—such as support vector machines (SVMs) and decision trees—which failed to achieve satisfactory accuracy, especially when the available input was limited to a reduced number of test sensors. In contrast, DNNs demonstrated a significantly improved ability to generalize the relationship between the anomaly index pattern and the underlying damage location, even in the presence of structural complexity and noise. Their flexibility and robustness make them a suitable and scalable solution for damage localization tasks in large-scale engineering structures.

Comprehensive details regarding the network architectures, dataset generation, and training strategy are provided in the dedicated case study section.

2.4. Integrated framework combining iFEM, anomaly index, and DNN for damage localization

The overall data-driven framework for localizing blast damage in ship structures is schematized and detailed in Fig. 3.

It consists of the following main steps:

- High fidelity simulation of an extreme event against the lateral side of a portion of a containership model, inducing hull plasticity and breakage. An explicit dynamic numerical framework is considered, comprehensive of a high-fidelity representation of the material's failure mode, capturing the realistic damage morphology.
- Creation of FE models with simplified damage: based on the extension of the damage obtained with high fidelity simulations, a simplified approach like the one proposed by Naval Society of Classifications is performed (Lloyd's Register, 2019), simulating the damage by removing the panels destroyed by the extreme event. This simplified model, assumed to be subjected to only one load correspondent to the longitudinal vertical bending moment, provides all the numerical strain measurements needed as input to the iFEM. A database of 270 analyses has been created, varying the location of the simulated damage on a two-dimensional grid located on the lateral side of the structure. The grid dimension was defined by considering the overall geometry of the structural component, the expected damage extension observed in typical failure scenarios, and the need to balance spatial resolution with computational efficiency.

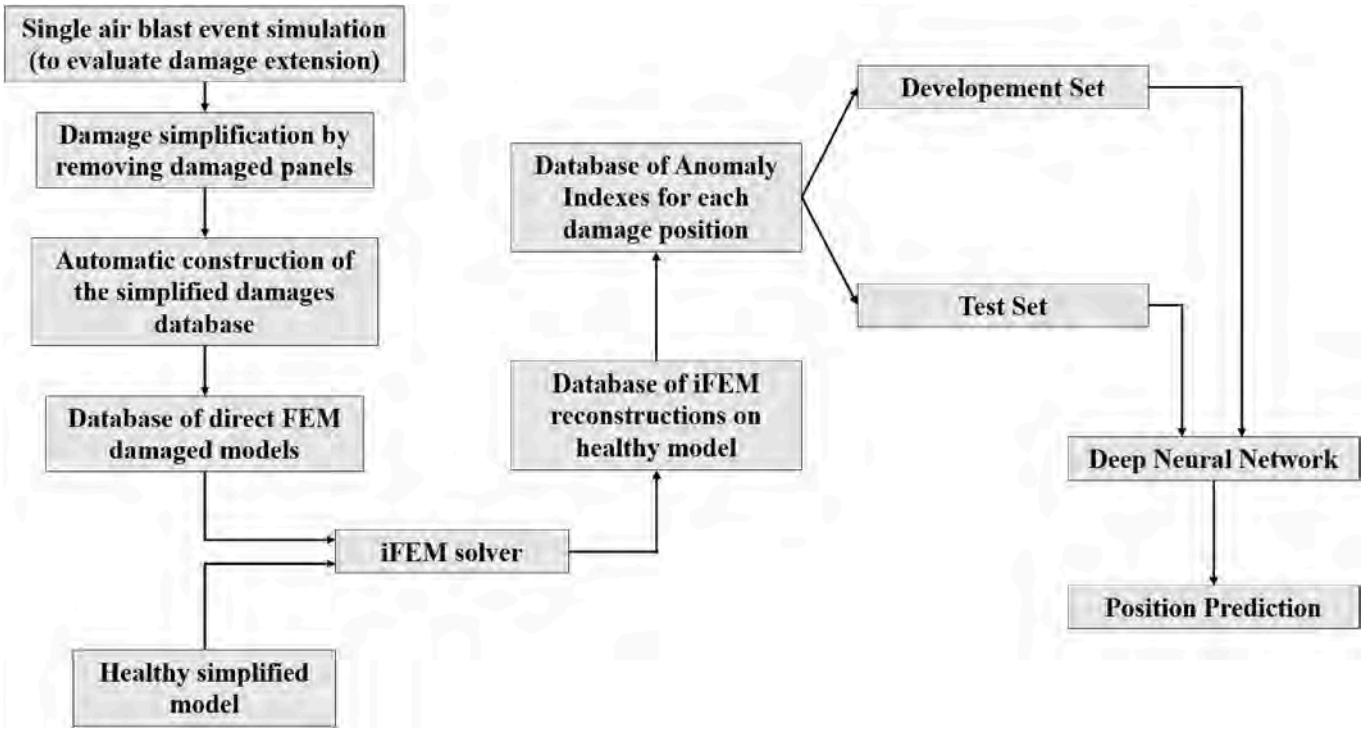

Fig. 3. Workflow chart of the framework implemented in the presented research.

- Creation of the healthy inverse FE model for full field displacement (and strain) reconstruction based on an FBG sensor network as input. The test sensor network for the calculation of the anomaly index is also defined and motivated in this step.
- Calculation of anomaly indices for damaged conditions: after the application of the iFEM algorithm on all simulated damaged cases, the anomaly indices are extracted and collected in a database.
- Implementation of the ML models: two DNNs are devised to identify the position of the damage through a regression task. The output of the DNNs is represented by the two coordinates defining the center of the damage position. Training, validation, and testing of the DNN is performed using the database of anomaly indices calculated based on numerical simulations in presence of simplified damages.
- Generalization capabilities: DNNs, trained with simplified damages, are tested with high-fidelity numerical simulations, verifying the potential of the method in real cases where a non-trivial morphology of the damage is present.

3. Numerical example on a containership model

This section contains a detailed description of the case study used. The structural assembly is described first, along with the FE model. Particulars of the extreme event analysis are provided, alongside a description of the simplified numerical model that emulates the real damage. Then, information about the inverse model, the sensor network and test sensor locations are provided. Finally, the data extraction process from iFEM results and the ML model are described.

3.1. Hi-Fi numerical FE model for air blast scenario

The present paragraph deals with the implementation of a high-fidelity numerical model regarding an extreme scenario against the lateral side of a containership, to evaluate the extension of the damage and then proceed on the definition of a simplified numerical model (Paragraph 3.2), comprehensive of a simulated damage, necessary for the creation of a large dataset. The geometry considered for the demonstration of the proposed framework corresponds to part of the double bottom of the midship region of a containership with length $L_{B.P.} = 353.0\,m$, breadth $B = 44.0\,m$, depth $D = 29.9\,m$ and designed draught $T = 14.5\,m$. This numerical model is inspired, with a representative level of geometric detail, by the MOL Comfort containership, a well-known benchmark vessel in structural research due to its documented structural failures (Bardiani et al., 2025c). Fig. 4 contains a schematic representation of the employed case study including the geometry as well as the applied load (only the longitudinal vertical bending moment for simplicity). In the interest of brevity, the reader is referred to (Aravanis et al., 2023) for detailed structural information which is not contained here; all NLFE calculations were made in ABAQUS CAE version 6.23 (Smith, 2009). Given the symmetry of the structure with respect to the diametral plane, only the right half of the section is studied here.

The FE model is composed of 115563 4-node quadrilateral shell elements with full integration. The average mesh size of the numerical model is 100 mm, while no refinement strategy has been adopted. The mesh size was determined after performing a mesh convergence process, to ensure that both displacements and stresses are accurately captured in the most important locations. The indication of the mesh used is

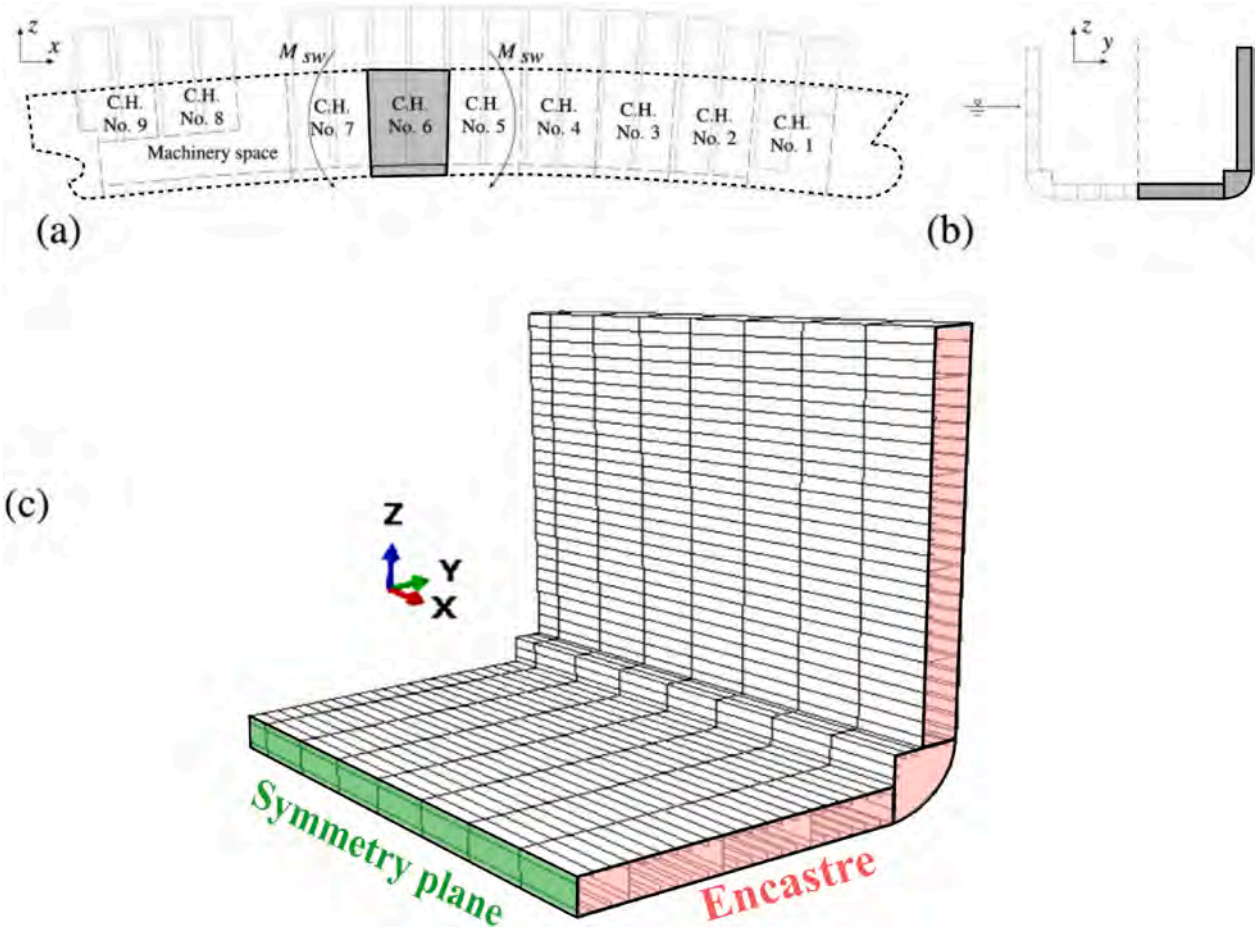

Fig. 4. 3D schematic representation of the benchmark case study under investigation (adapted from (Aravanis et al., 2023)).

reported in Fig. 5a.

Regarding the material, typical naval mild steel properties are used, namely $E = 209\ MPa$, Poisson's ratio $\upsilon = 0.3$ and density $\rho = 7850\ kg/m^3$ (Ehlers et al., 2008; Prabowo et al., 2022). The plastic behavior of the material is modelled using the Johnson-Cook law, with parameters as shown in Table 1 (Johnson, 1983; Lin et al., 2014), where A represents yield stress, B is the strain hardening coefficient, n represents the hardening index, C is the rate hardening coefficient, m is the temperature softening coefficient, $\dot{\varepsilon}_0$ is the reference strain rate, T_{ROOM} is the room temperature and finally T_M is the melting temperature.

Structural damage behavior is considered, using the Rice-Tracey and Cockcroft-Latham (RTCL) damage model (Simonsen and Törnqvist, 2004). It is a specific ductile failure criterion based on the combination of two models for predicting ductile failure: the Cockcroft-Latham criterion, which addresses ductile shear fracture or more broadly the low triaxialities range, and the Rice-Tracey criterion ((Rice and Tracey, 1969)), which is based on void growth and coalescence and is more suitable for high triaxialities. It consists of the following formulation (Simonsen and Törnqvist, 2004):

$$D_i = \frac{1}{\varepsilon_0} \cdot \int f\left(\frac{\sigma_H}{\sigma_{eq}}\right)_{RTCL} d\varepsilon_{eq}^p \tag{8}$$

In which:

$$f\left(\frac{\sigma_H}{\sigma_{eq}}\right)_{RTCL} = \begin{cases} 0, for\ \frac{\sigma_H}{\sigma_{eq}} \le -\frac{1}{3} \\ 2 \cdot \frac{1 + \frac{\sigma_H}{\sigma_{eq}} \cdot \sqrt{12 - 27 \cdot \left(\frac{\sigma_H}{\sigma_{eq}}\right)^2}}{3 \cdot \frac{\sigma_H}{\sigma_{eq}} + \sqrt{12 - 27 \cdot \left(\frac{\sigma_H}{\sigma_{eq}}\right)^2}}, for\ -\frac{1}{3} < \frac{\sigma_H}{\sigma_{eq}} < \frac{1}{3} \\ \frac{1}{1.65} \cdot e^{\frac{3}{2}\frac{\sigma_H}{\sigma_{eq}}}, for\ \frac{\sigma_H}{\sigma_{eq}} \ge \frac{1}{3} \end{cases} \tag{9}$$

More specifically, D_i is the normalized ductile failure damage indicator, ε_0 represents the damage strain parameter, σ_H is the hydrostatic stress, σ_{eq} is the equivalent von Mises stress, while $d\varepsilon_{eq}^p$ represents the effective plastic strain increment. The RTCL damage model is sensitive to the size of the mesh; for this reason, the following equation has been proposed to determine the parameter ε_0, which is the only parameter necessary to implement the criterion:

Table 1
Material parameters used in numerical simulation (values taken from (Lin et al., 2014)).

$A[MPa]$	$B[MPa]$	$n[\ -\ ]$	$C[\ -\ ]$	$\dot{\varepsilon}_0[s^{-1}]$	$m[\ -\ ]$	$T_{ROOM}[K]$	$T_M[K]$
490.0	600.00	0.210	0.015	1.0	0.60	293	1800

$$\varepsilon_0\left(\frac{t}{l_e}\right) = \mathrm{n} + (\varepsilon_n - n) \cdot \frac{t}{l_e} \tag{10}$$

Where l_e is the mesh element size (100 mm in the present case), t is the structural element size (thickness of the bottom plate, to have the lowest value of $\frac{t}{l_e}$), ε_n is the failure strain at $\frac{t}{l_e} = 1$ for uniaxial strain (taken from (Ehlers et al., 2008)) and n is the power law coefficient. The values listed in Table 2 have been considered for all analyses performed in this work.

According to the RTCL model, if during the analysis some finite elements reach a damage $D_i = 1$ (i.e. the failure criterion value), they will be considered as totally damaged and removed from the calculation. The choice of boundary conditions is described in Fig. 4 and no other information on it is reported here for simplicity.

The extreme scenario considered in this study is visually reported in Fig. 5b. A blast load, resulting from a sudden release of energy in the form of a detonation or deflagration, generates a highly compressed gas mass that interacts with the surrounding air, producing an outward-propagating shock wave (i.e., pressure waves). Such extreme loading conditions can originate from various sources, including accidental gas leaks near oil and gas platforms, industrial accidents, or even collisions involving vessels or infrastructure. A typical incident pressure history of this kind of pressure load is shown in Fig. 6, derived through the application of the Friedlander equation (Draganić and Sigmund, 2012).

Severity of blast waves, generated by the explosion event, obey a cube-root scaling, known as Hopkinson-Cranz law:

Table 2
Identification of the parameters of the steel used within the Rice-Tracey and Cookcroft-Latham criteria (RTCL).

$l_e[mm]$	$t[mm]$	$\frac{t}{l_e}[\ -\ ]$	$n[\ -\ ]$	$\varepsilon_n[\ -\ ]$	$\varepsilon_0[\ -\ ]$
100	20	0.2	0.20	0.67	0.294

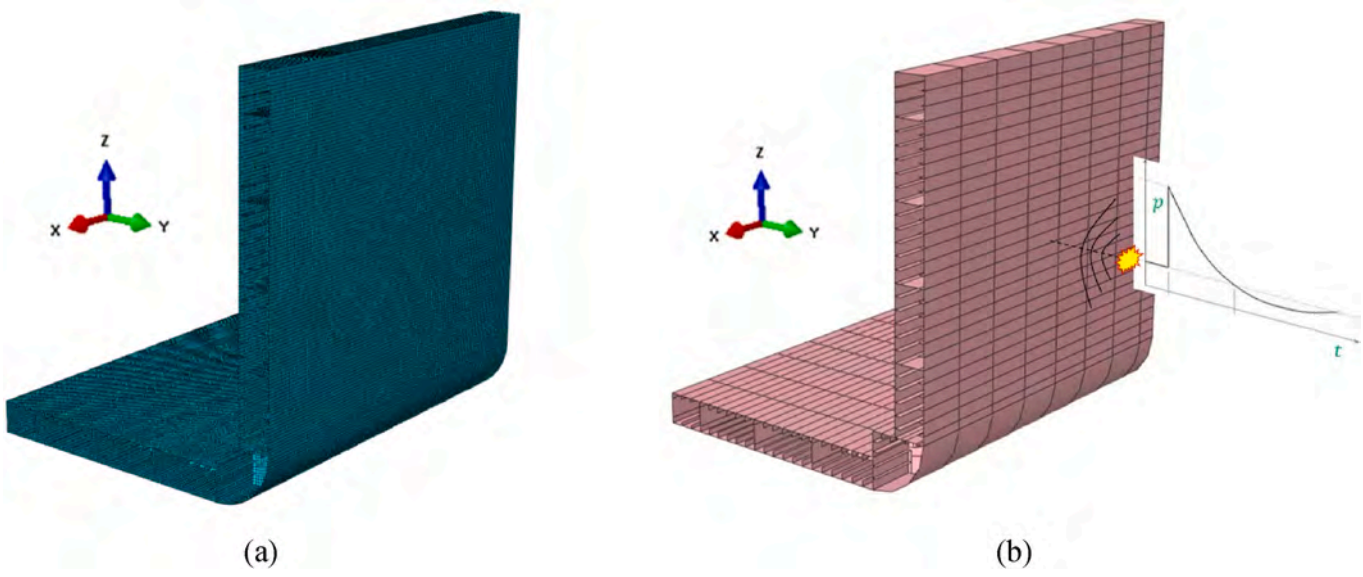

Fig. 5. Explanation of the main features of FE model: (a) mesh and (b) extreme scenario configuration.

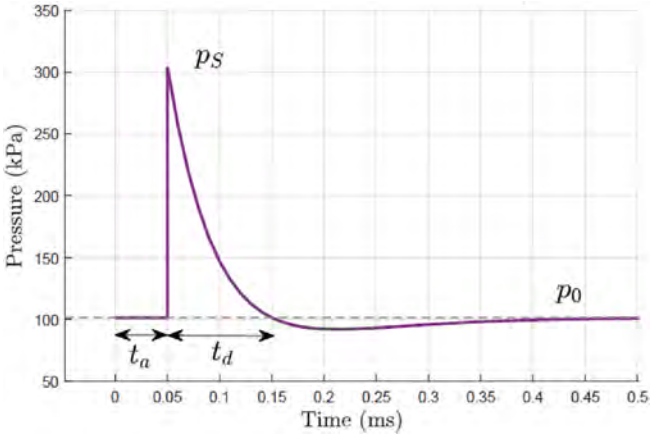

Fig. 6. Typical pressure history of a blast wave in an unconfined environment: pressure-time diagram due to the application of Friedlander equation.

$$Z = \frac{R}{\sqrt[3]{M}} \tag{11}$$

In which R is the stand-off distance in meters, M is the TNT-equivalent explosive charge mass expressed in kg and Z represents the scale distance in $m/kg^{1/3}$.

Kingery and Bulmash (1984) reported tables with empirical curves obtained from experimental campaigns. The loading effects due to this blast event in air can be defined, for spherical incident waves or hemispherical incident waves, by the CONWEP computational framework (CONventional Weapons Effects Program) based on Kingery-Bulshman curves, in conjunction with the incident wave loading definition. The CONWEP algorithm, which is directly implemented as an option in the commercial finite element software ABAQUS/Explicit and is widely adopted in the literature for blast analyses, was employed in the present study.

For this study, it was decided to use the values $R = 3.0\,m$ and $M = 10\,kg$, to obtain $Z = 1.39\,m/kg^{1/3}$, in order to comply with the validity range and assumptions of the Kingery–Bulmash method as reported in Kingery and Bulmash (1984).

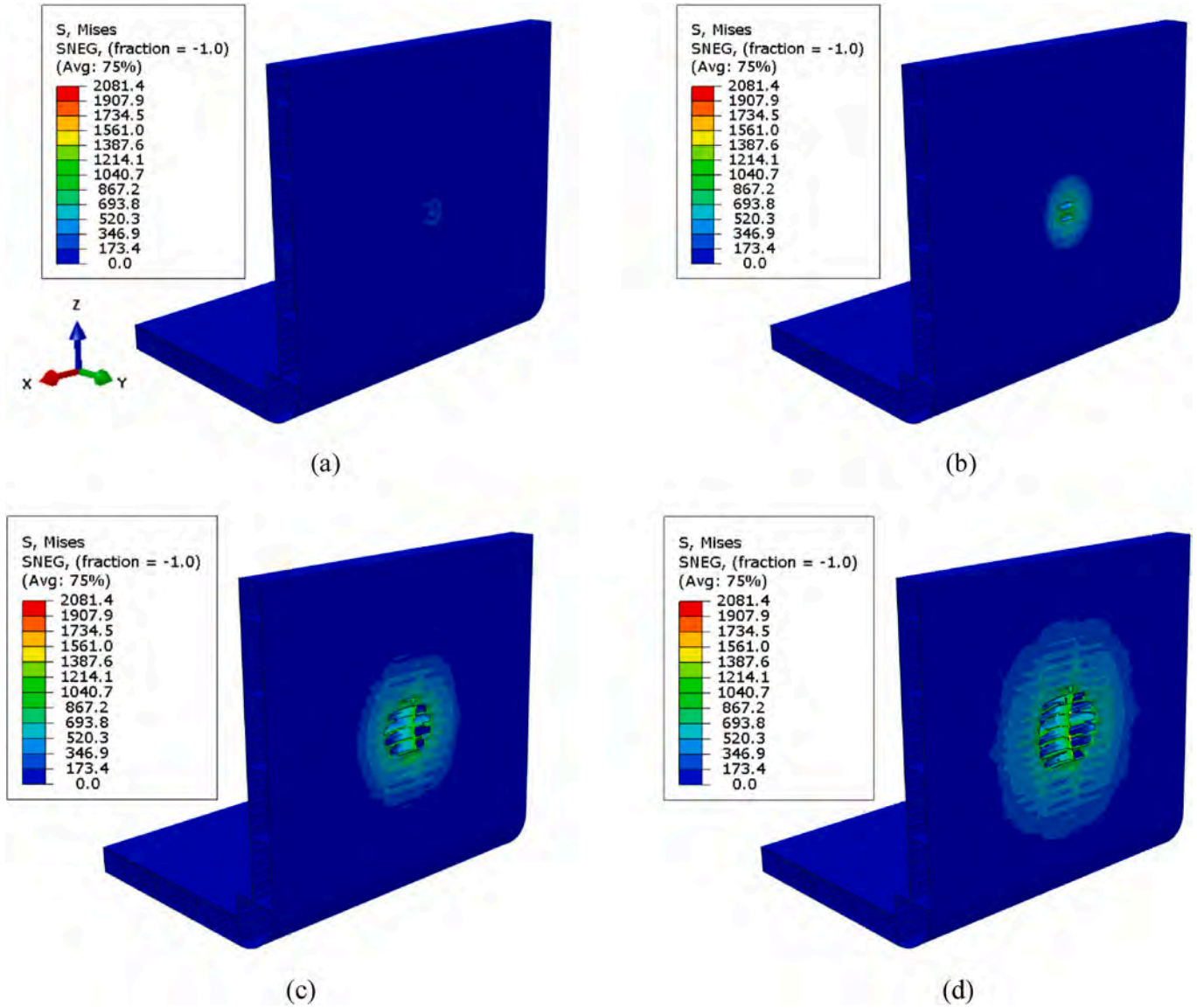

Fig. 7. Von Mises stress distribution (in MPa) of the structure under the action of the blast scenario at different time (deformation scale factor: 1, mesh shaded): (a) t = $3.75{\cdot}10^{-4}$ [s], (b) t = $8{\cdot}10^{-4}$ [s], (c) t = $14{\cdot}10^{-3}$ [s] and (d) t = $20{\cdot}10^{-3}$ [s] (used same legend and same reference system).

Analysis time was set to $t = 0.020\ s$ to reach the maximum damage that occurs on the structure, while the time of detonation is $t = 0.0\ s$. Finally, based on the global reference system of the numerical model presented in Fig. 4, the detonation point in located at $x = -13.5\ m$, $y = 7.0\ m$ and $z = 14.0\ m$ (see Fig. 5b for better clarity). In Fig. 7, the contour plots of the Von Mises stress fields of the structure under examination are shown, in four different time instants.

Fig. 8 shows a magnification of Fig. 7d with a detailed view on the damaged area, characterized by a highly complex damage morphology. To handle this complexity and to reduce the computing request to create a dataset of simulations needed for the ML training, a simplified approach was necessary and described in detail in Paragraph 3.2, coherent with the approach proposed in (Lloyd's Register, 2019) described in the next section.

3.2. Simplified FE direct model

This section describes the numerical model (called "direct") from which the strains to be provided as input to the iFEM code are taken. As previously described, the direct model presents damage induced by an extreme event (Fig. 8), accurately simulated through the CONWEP tool of ABAQUS CAE. In the present framework, since it was necessary to create a big dataset containing several models with different locations of the damage, the approach of running all dynamic explicit simulations is not convenient. Starting from the simulations performed in Paragraph 3.1, simplified damage is approximated as a square opening on the ship's side, removing the external planking, the horizontal and vertical stiffeners affected by the extreme event, as shown in Fig. 9a.

The authors point out that this approach, albeit with some different facets, is the one proposed by some societies of classification to consider the threat of damage on the hull. For instance, Loyd's Register proposes the definition of a cylinder of appropriate size (to be positioned in the more unfavorable position for the structures) that cuts part of the hull inducing a reduction in structural integrity (Loyd's Register, 2019). Once this is done, the damaged ship should be simulated in a static environment, with its cargoes, verifying whether the loss of structural integrity induces permissible stress conditions for the ship. In this approach, the definition of damage is certainly a great simplification, and aims to mimic the effect of the damage on the structure only in a phenomenological way.

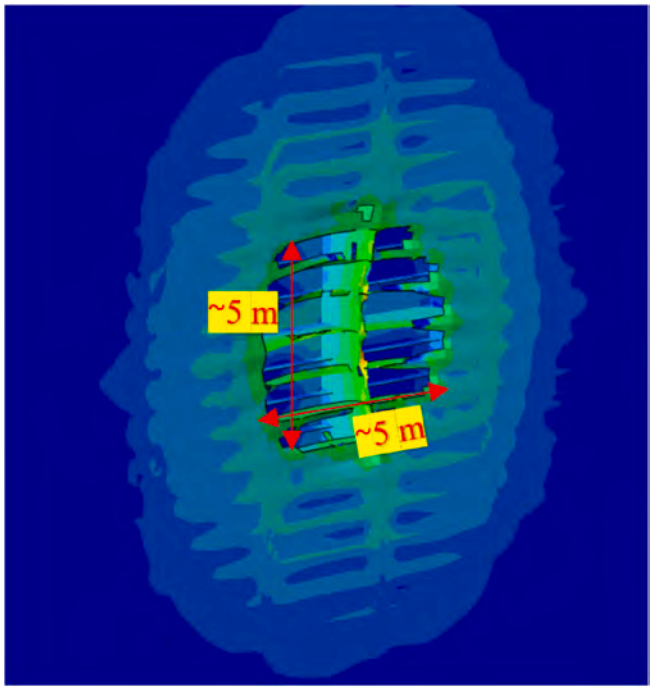

Fig. 8. Magnification of the damaged area of the structure under investigation at t = $20{\cdot}10^{-4}$ [s], with the indication of the main dimensions.

The present framework enhances the accuracy of the previous method, since the real portions of structures that have been affected by the explosive phenomenon are erased from the model, making the simulated damage extremely truthful and significantly reducing the major simplifications of the Society of Classification Rules.

Two examples of "direct" models are given in Fig. 9. Fig. 9a proposes a visual representation of the simulated damage on the hull corresponding to the Hi-Fi one of Fig. 7d.

All the direct models present the same geometry, material and BCs with respect to the model presented in Fig. 4, apart from three main aspects following highlighted.

The first one is related to the fact that they present simulated damages, but at different locations. The extent of damage is derived from Fig. 8 (5 m squared). The second aspect regards the implementation of the iFEM algorithm: since the code used in the present investigation works for small and elastic displacements (Kefal et al., 2016), neither plastic nor damage behavior has been implemented. Finally, the third difference is related to the load applied to the model: while in the previous case an extreme event was the only load implemented, here the load is a longitudinal vertical bending moment acting on the hull, applied to a MPC (type beam) located to the center of gravity of the right external section of the model (Fig. 10a, Salazar-Domínguez et al., 2021). Since only half of the model has been implemented, given the symmetry with respect to the diametral plane, the moment calculated with the formulas below has been halved accordingly.

Since precise information about all the weight and loads of the model under investigation were not available, the calculation of the longitudinal vertical bending moment acting on the hull was possible through the implementation of empirical formulations proposed by International Association of Classification Societies (IACS) (Iacs, 2024). It has defined empirically formulas through which, thanks to a few simple parameters, it is possible to determine the vertical bending moment, both on sagging and hogging, in such a way as to consider the entire length of the ship. The equation used here for the sagging load condition is the following:

$$M_{WV,S} = -110{\cdot}F_M \cdot n \cdot C{\cdot}L^2 \cdot B \cdot (C_B + 0.7) \cdot 10^{-3} = 4.5{\cdot}10^9\ [kNm] \qquad (12)$$

Where F_M (equal to 1) is the factor of distribution of the bending moment over the length of the ship and can be obtained from tables, n equal to 1 is the navigation constant (from tables), C is the wave parameter (equal to 10.75), L is the sizing length of the vessel in meter ($=L_{B.P.}$), B is the maximum width out of the frame amidships (already defined) while $C_B = 0.7$ is the total fineness coefficient of the vessel, calculated out of planking, therefore including the factor $k_C = 1.006$.

An example of a result of the "direct" model, for what concerns ε_{11} strain results, is presented in Fig. 10b. Also, Fig. 10c presents the ε_{11} strain pattern in the model without any damage, to appreciate its difference with respect to Fig. 10b.

As expected, the damaged structure exhibits a strain field noticeably altered with respect to the healthy case, and it is precisely this discrepancy that forms the basis for computing the anomaly index values.

3.3. The iFEM model

The iFEM model is presented in Fig. 11a and it consists of 7153 iQS4 elements and the boundary conditions imposed are the same presented in Fig. 4. The choice of the mesh size of this model was properly defined based on the accuracy of the displacement reconstruction and on the computational cost associated with the iFEM code. As anticipated in Paragraph 2, no information on load and material property is passed to the iFEM for full displacement and strain field reconstructions. In this study, the reconstruction of the displacement field is carried out with

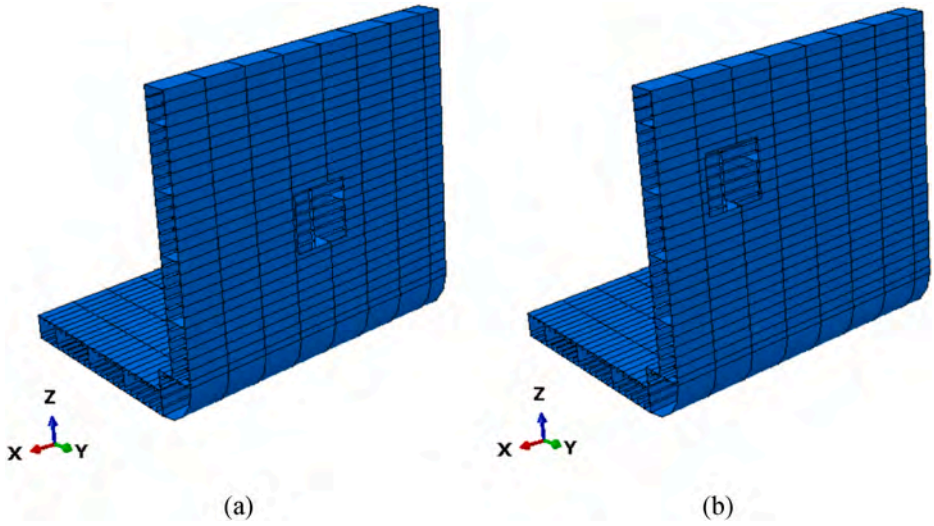

Fig. 9. Visualization of two different "direct" models, with different damage locations.

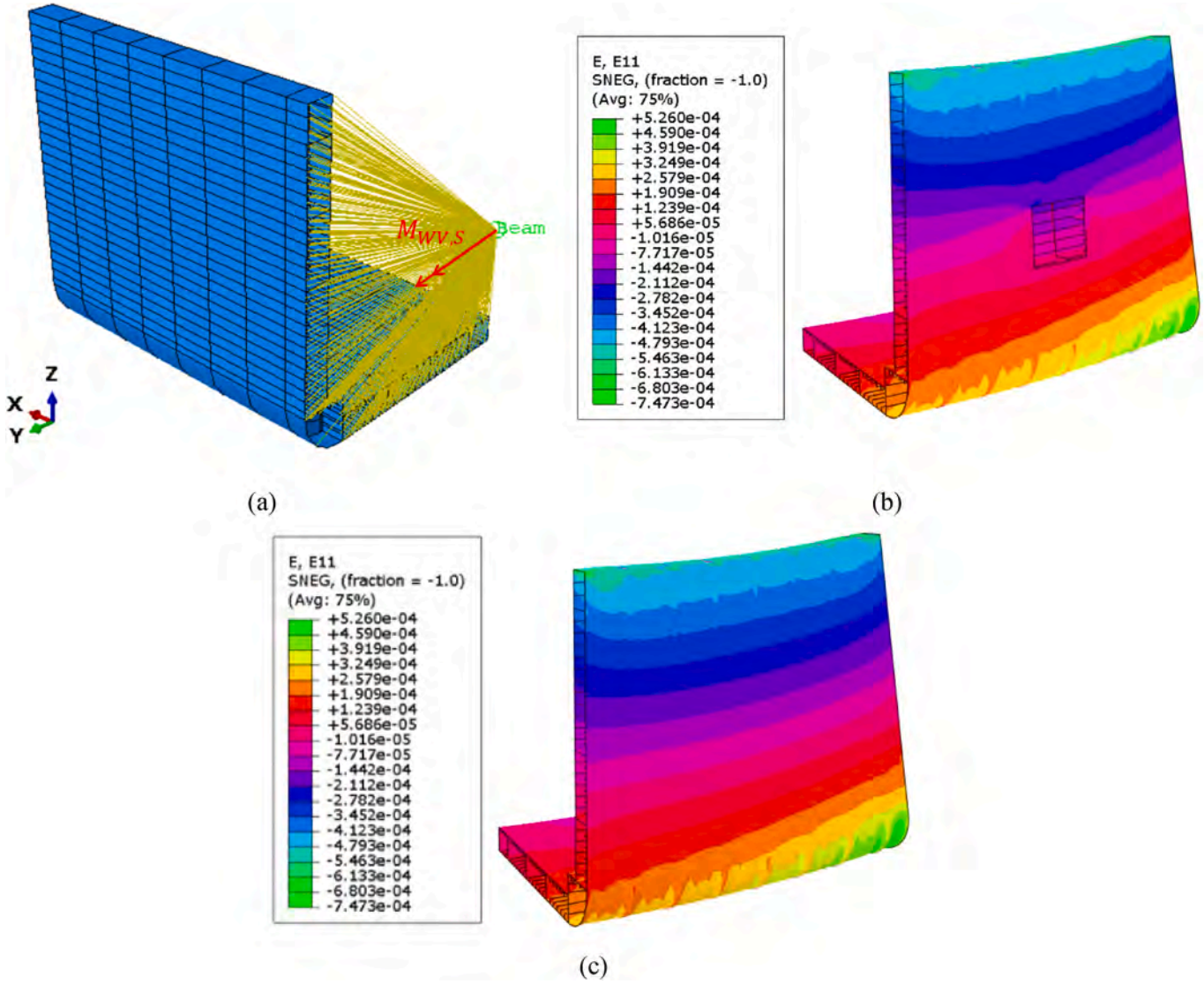

Fig. 10. Direct model features: (a) implementation of the MPC for the bending action, (b) example of ε_{11} strain results and (c) ε_{11} strain contour in the model without damage.

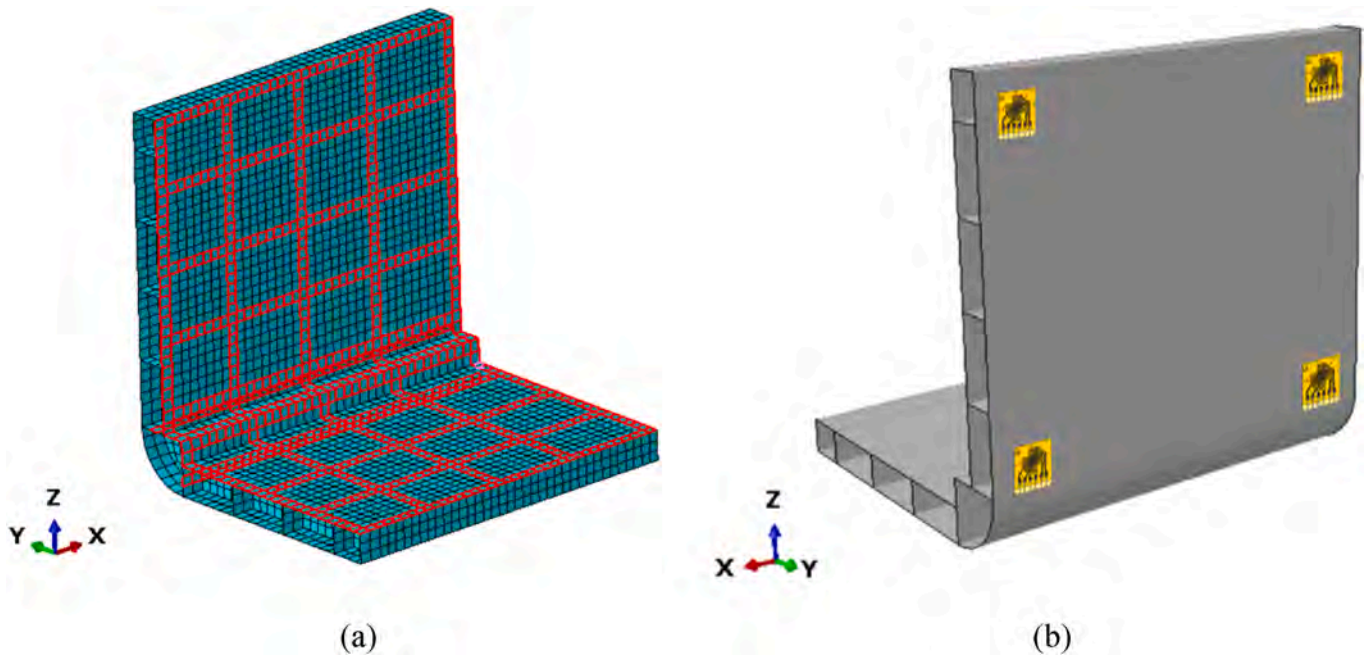

Fig. 11. Inverse model features: (a) FBG-based sensor network and (b) rosettes-based test locations for Anomaly Index calculation.

iFEM only using numerical measurements taken from the "direct" numerical FE model described in Paragraph 3.2. The important aspect of the inverse FE model is the definition and implementation of the sensor network and position of test sensors, latter necessary for anomaly index calculations.

As shown in Fig. 11a, the FBG-based sensor network used within the structure can be potentially applied in real scenarios and, in particular, it is located on both surfaces of the inner wall of the containership, to avoid issues with the external water environment. Moreover, this network is not directly affected by the damage, since the extreme event load induces major damage on the external plating of the hull and on the structural elements welded to it, but not on the inner side wall. Several FBG sensor configurations have been tested, and the one presented here represents the most promising solution, as it allows the best performance in the reconstruction of the full field of displacement. The choice of this sensor layout was the outcome of preliminary analyses specifically aimed at identifying an optimal compromise in terms of installation cost, reconstruction accuracy, compliance with physical and operational constraints, and robustness to environmental conditions (Bardiani et al., 2025a). These considerations make the proposed sensor network and case study highly realistic and applicable to full-size structures.

As for the test sensors (for simplicity strain gauge rosettes with triple value provided ε_{11}, ε_{22} and γ_{12}), necessary to calculate the anomaly index values, they are positioned as shown in Fig. 11b. It is important to underline that their number is extremely limited (only 4), making the framework very interesting to test on real structures.

There are no strict or universally accepted rules for determining the number and placement of test sensors within the anomaly index framework (Colombo et al., 2021). Their configuration must instead be defined case by case, depending on the geometry of the structure, the type of damage expected, and the physical and economic constraints of the application. In this study, the choice of employing only four test sensors is the result of a trade-off between accuracy, cost, and practical feasibility. In preliminary analyses, different sensor configurations were investigated, ranging from denser to sparser layouts, to evaluate their effect on the performance of the anomaly index. Increasing the number of test sensors beyond four provides only marginal improvements in the ability to capture localized variations of the strain field and to refine the anomaly index distribution, while it substantially increases the complexity of the SHM system, installation costs, and the amount of data to be processed. Conversely, employing fewer than four test sensors markedly reduces both the sensitivity and robustness of the framework, as the limited number of measurement points would be insufficient to capture the localized variations in the strain field induced by damage.

Another important aspect is that the anomaly index values computed at the test sensor locations are subsequently used as input features for ML models. A denser test sensor network would increase the dimensionality of the input space, which in turn requires a much larger training dataset to avoid overfitting and to ensure generalization. This would significantly raise computational costs both in dataset generation (more simulations) and in the training phase, undermining the scalability of the method. By limiting the number of test sensors to four, the input space is kept compact, facilitating efficient and reliable DNN training while still ensuring that the anomaly index retains sufficient discriminatory capability to localize damage. In this sense, the selection of four sensors not only reduces hardware and installation costs but also optimizes the balance between physical measurements and ML performance.

The physical placement of the sensors also reflects this rationale: the four strain gauge rosettes are located close to the corners of the outer lateral plating on the inner side of the hull. This arrangement ensures that they capture strain variations induced by damage across the entire plate region, while remaining protected from direct seawater exposure. Their distribution provides a wide coverage of the structural domain of interest, enhancing the sensitivity of the anomaly index to localized incompatibilities without requiring a dense sensor grid.

Finally, robustness to sensor failure was also considered: with four sensors strategically distributed, the framework maintains functionality even in the event of a single sensor malfunction, ensuring fault tolerance without compromising sensitivity. This makes the proposed configuration both practical and resilient, while fully compatible with the subsequent data-driven damage localization stage.

As already mentioned in Paragraph 2, to enhance the accuracy of iFEM results, the input strain field has been extrapolated into element locations where physical sensors are absent, so outside the sensor network path of Fig. 11a. In this case, the problem of the choice of the weight to be put inside the weight matrix $\boldsymbol{W}$ has been addressed. In particular, the best configuration reveals a unitary value of weight to

elements where the input strain field component is measured by physical sensors, value of 10^{-4} for missing in-situ strain component elements and 10^{-3} for the pre-extrapolated ones. For simplicity, a third-order polynomial fit was applied for pre-extrapolation on the sensorized surfaces in both orthogonal directions of the local coordinate system. Fig. 12 provides all the results of a generic representative case scenario within the dataset, with the indication of the damage's position. The authors point out that all the plots within Fig. 12 correspond to the global reference system of Fig. 12a.

As shown in Fig. 12, the full field of displacement reconstructed by the iFEM (Fig. 12c) is in good agreement with the numerical values regarding the "direct" model (Fig. 12b), with the simulated damage indicated in Fig. 12a. The results of the iFEM reconstructions are in line with what expected, symptoms of a correct choice and design of the FBG-based sensor network together with the pre-extrapolation strategy.

Fig. 12d shows the percentage total error magnitude of the reconstructed displacement field of the ship portion under investigation. This plot highlights only local error peaks of less than 7 % in specific zones near the model boundaries and this result does not noticeably vary with the change in the damage position. It's important to notice that the inverse model does not contain any information regarding the damage presence or position and the reconstruction is carried out completely independently from that. The iFEM model keeps in the reconstruction all the elements of the undamaged structure, also the ones destroyed by the extreme event: the removed elements in Fig. 12b–d corresponding to the position of the damage in the direct FEM model are manually removed

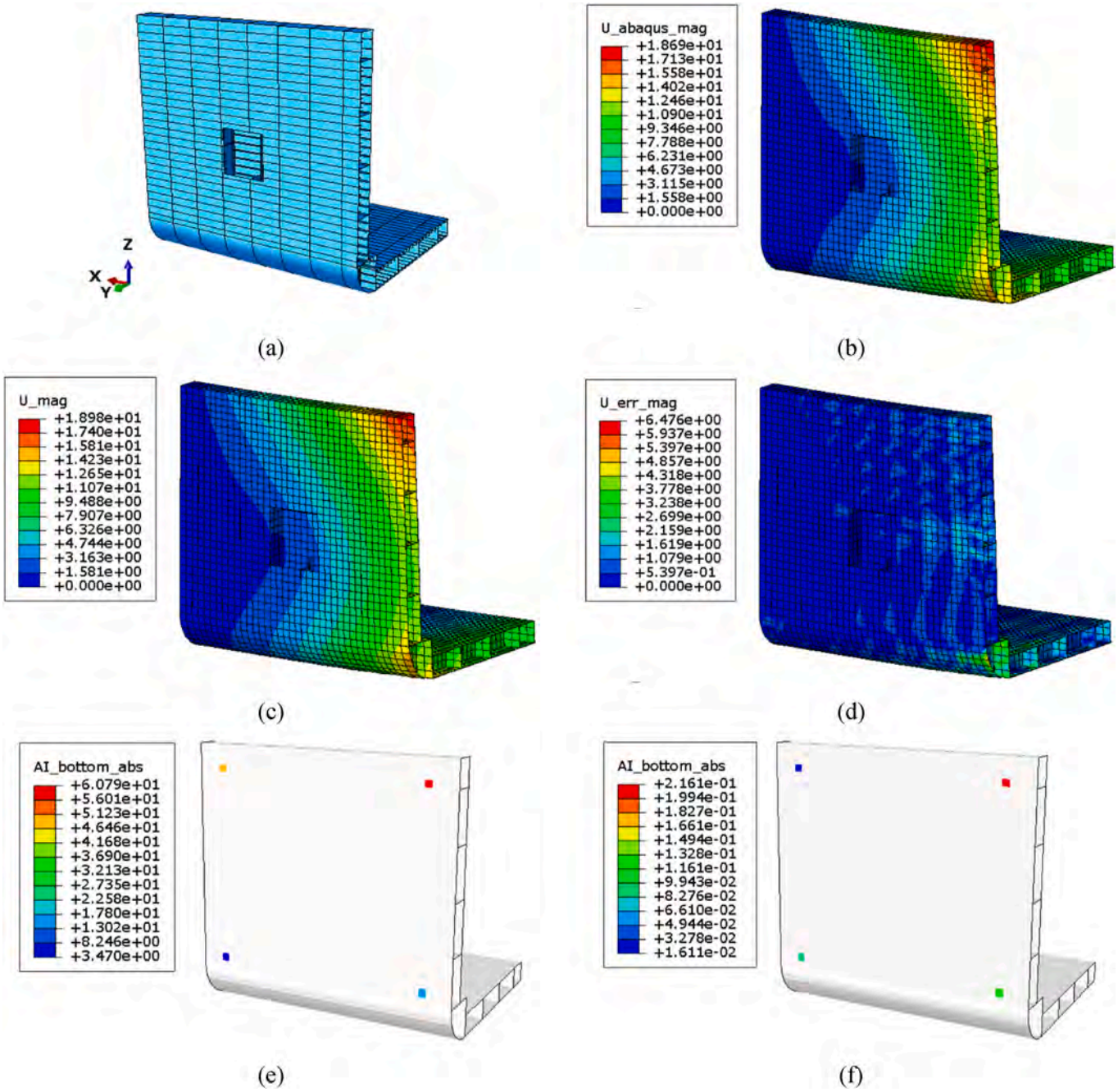

Fig. 12. Results provided by the iFEM code for a representative case inside the dataset: (a) direct FE model with the damage, (b) total displacements of the direct FE model (in mm), (c) total displacements reconstructed by iFEM (in mm), (d) percentage error between the real and reconstructed value of the displacement (%), (e) Anomaly Index plot calculated for the rosettes-based test locations and (f) Anomaly Index plot in the case of healthy state.

after the reconstruction only for graphic purposes, to allow clear plot of the results' error.

In Fig. 12e is shown the anomaly index absolute value plot for the four test sensors located in the corner of the external side plating of the ship portion (see Fig. 11b). This anomaly index plot certainly proves the presence of anomalies in the state of health of the structure, since in the test sensor locations there are high values of $i(\boldsymbol{x}_t)$ with respect to the one obtained from a healthy structure without any damages (Fig. 12f). Despite this, it is evident that from this pattern (Fig. 12e) that it not possible to precisely locate the point where the structure is damaged, due to the strong non-linear behavior of this index. To overcome this issue, as mentioned, two ML models are introduced within the framework.

3.4. Data extraction to create the dataset

For the dataset generation step, all iFEM simulations of Paragraph 3.3 underwent a post-processing procedure to extract appropriate data describing the anomaly index values in the sensor test locations ($\boldsymbol{i}(\boldsymbol{x}_t)$). In particular, the strain components ε_{xx}, ε_{yy} and γ_{xy} are extracted from the four test sensors located on the lateral side of the structure (12 anomaly index values overall for each simulation).

The dataset is composed of 270 simulations, obtained by varying the position of the center of damage over the entire lateral surface of the structure. Based on the grid in Fig. 15, the center of damage is shifted by 800 mm in both directions of the plot, obtaining a total of 270 cases. This shifting step was chosen as a compromise between spatial resolution and computational feasibility: a smaller step would have generated a denser grid and a significantly larger number of simulations, which would have been computationally demanding, while a larger step would have excessively coarsened the grid, reducing the ability to capture localized variations in the strain field induced by damage. The selected 800 mm spacing therefore ensures sufficient variability of damage scenarios to train the ML models, while keeping the dataset size manageable. It should be emphasized that the choice of the shifting step—and consequently the number of simulations to be performed—ultimately depends on the user of the tool, their available computational resources, and the level of accuracy desired in the damage localization process. In this sense, the framework is flexible and can be adapted to different operational needs and constraints. It is also worth noting that, in the naval field, unlike in other engineering applications such as aerospace or precision mechanical systems, a millimetric accuracy in identifying the damage location is not necessarily required. In practice, what is more relevant for decision-making is the ability to identify the damaged compartment, or the specific zone within a compartment, rather than the exact point where the structural failure originated.

3.5. The machine learning model

For the data-driven step, a set of two feed-forward DNNs were implemented and optimized. The DNNs were deployed, trained, and assessed using the PyTorch library, coded in Python. The architectures used in this study for predicting the coordinates of the center of structural damage were carefully designed to capture the complex relationships encoded in the Anomaly Index values obtained from the test sensors shown in Fig. 11b. In particular, one DNN was trained to predict the X coordinate, while a second DNN was trained to predict the Y coordinate of the damage location (reference system of Fig. 13, left). Various DNN architectures were explored during the development process; however, to keep the discussion concise, only the most effective

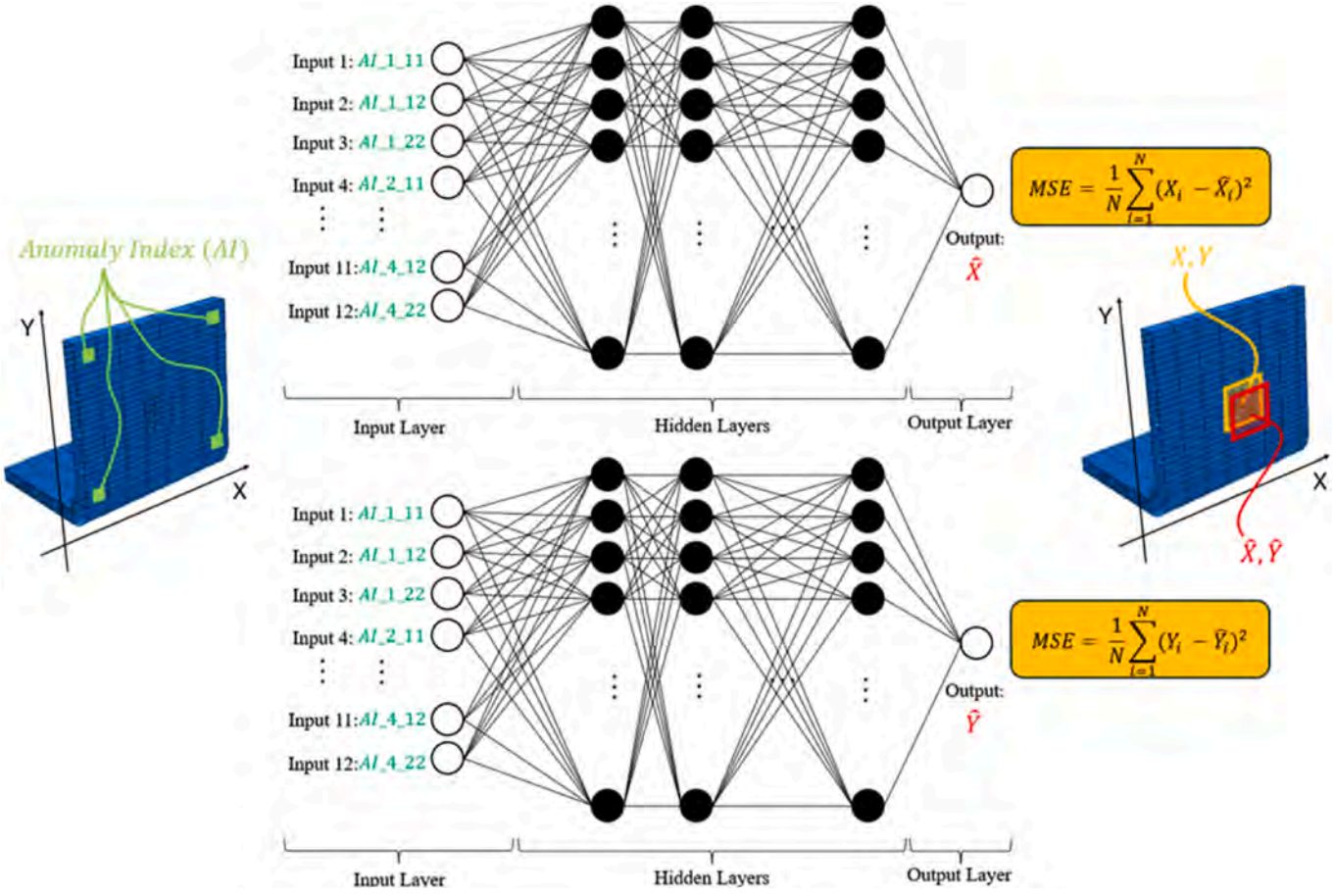

Fig. 13. Schematic diagram of the DNN model of the present framework.

configuration is presented.

The schematic diagram of the NNs implemented in this work is shown in Fig. 13, while the main characteristics of architecture are summarized below. Both DNNs comprise multiple hidden layers, each containing a substantial number of neurons to ensure sufficient learning capacity, as already indicated in Section 2.3. Specifically, each model includes: (i) an input layer with 12 neurons, corresponding to the 12 input features (three strain components, ε_{xx}, ε_{yy} and γ_{xy}, from each of the four test sensors), (ii) four hidden layers with 64 neurons each, representing a balance between expressive power and computational feasibility, and (iii) an output layer consisting of a single neuron, which returns the predicted continuous value for either the X or Y coordinate of the damage center.

Among the numerous optimization challenges in deep learning, the training phase of NNs is often the most delicate and critical. A key step in this process involves the preparation of the dataset, which must be structured to allow both effective learning and reliable performance assessment. To this end, the available dataset was randomly divided into three distinct subsets: a training set, used by the network to adjust its weights and biases; a validation set, employed during training to monitor convergence and tune hyperparameters, thereby reducing the risk of overfitting; and a test set, reserved exclusively for the final evaluation of the model's generalization capability on unseen data (Zhou, 2021). The subdivision of the dataset followed the commonly adopted proportions for ML applications (Bardiani et al., 2025b), and the resulting partitioning into training, validation, and test sets is clearly illustrated in the schematic of Fig. 14.

The spatial distribution of the damage cases included in the dataset is shown in Fig. 15. Each point, representing the center of a simulated damage, is color-coded according to its assignment to the training, validation, or test set. For clarity, the same figure also illustrates the extension of the damaged area corresponding to a representative damage center.

An essential aspect of DNN implementation involves the definition of the training procedure, which requires selecting a loss function, an optimizer, and an appropriate activation function, since these components strongly affect both training efficiency and predictive accuracy. In this work, the chosen loss function is the mean squared error (MSE), which quantifies the discrepancy between predicted and actual coordinates of the damage center. Its formulation is reported in Fig. 13 inside the orange boxes. The Adam optimizer was adopted for parameter updates, as it is known for its robustness and efficiency in handling nonlinear regression problems (Hinton et al., 2006).

The dataset was used to train the networks for 100 epochs. This value was selected after preliminary experiments in which different epoch numbers were tested while monitoring validation error: 100 epochs provided the most stable convergence without overfitting. The batch size was set to 32, a commonly used compromise that balances the stochastic nature of mini-batch gradient descent with the stability of full-batch training.

To enhance the generalization capability of the model and prevent overfitting, several regularization strategies were introduced. First, dropout layers were applied, with a rate of 20 % for the X-coordinate model and 30 % for the Y-coordinate model. Dropout is a widely used technique in deep learning, in which a random subset of neurons is temporarily deactivated during each training iteration. This prevents neurons from co-adapting excessively and forces the network to develop more robust and generalizable internal representations of the input data. The chosen dropout rates were determined through a hyperparameter tuning process: smaller values (10–15 %) proved insufficient to mitigate overfitting, whereas higher values (>40 %) resulted in unstable convergence and accuracy degradation. The slightly stronger dropout adopted for the Y model reflects the higher variance observed during its training process, which required stronger regularization. In addition to dropout, L2 regularization was applied to each dense layer of the network. This technique penalizes excessively large weights in the loss function, discouraging overly complex solutions and promoting smoother and more stable mappings between input features and output predictions.

Finally, activation functions play a fundamental role in enabling the network to capture nonlinear relationships (Zhou, 2021). Several options were tested, including ReLU, sigmoid, tanh, and softmax. Among these, the rectified linear unit (ReLU) consistently provided the best results in terms of accuracy and stability. ReLU was therefore adopted in all hidden layers, as it allows neurons to remain active throughout training and prevents vanishing gradient issues, thereby facilitating efficient learning of complex patterns.

3.6. Generalization capability for real cases

The ML models developed in Paragraph 3.5 were originally trained on anomaly index values obtained from iFEM reconstructions in which the inputs derived from a direct numerical model with simplified, idealized damage geometries (Fig. 9). While this setup allowed the creation of a sufficiently large and consistent dataset for training and validation, it does not fully reflect the complexity of realistic damage patterns.

To verify the actual potential of the proposed approach, an additional assessment was therefore carried out, aimed at testing the predictive capabilities of the DNNs in the presence of more realistic, non-simplified damage scenarios. These scenarios were generated using the high-fidelity extreme load simulations described in Paragraph 3.1, which provide a more detailed and physically representative characterization of structural damage following an extreme event.

This additional validation step was crucial for two reasons. First, it allowed us to evaluate whether the trained networks could generalize beyond the simplified assumptions used during training and still deliver accurate localization results. Second, it provided a first indication of the robustness and applicability of the proposed framework to real-world naval structures, where damage is rarely idealized and often exhibits complex geometrical features and interactions with the surrounding structure.

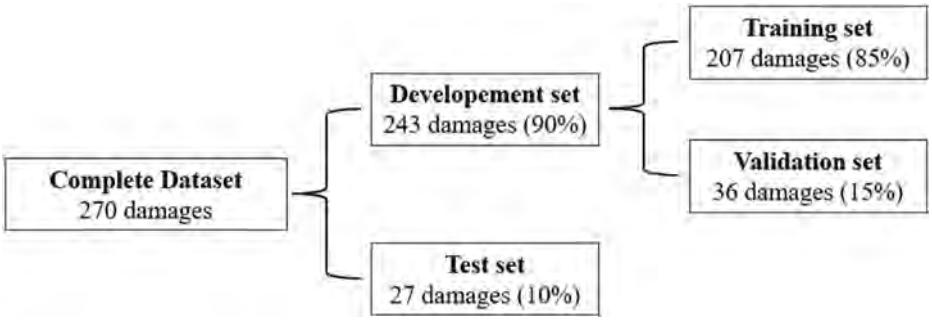

Fig. 14. Dataset subdivision regarding simulated damage numerical models of Paragraph 4.2.

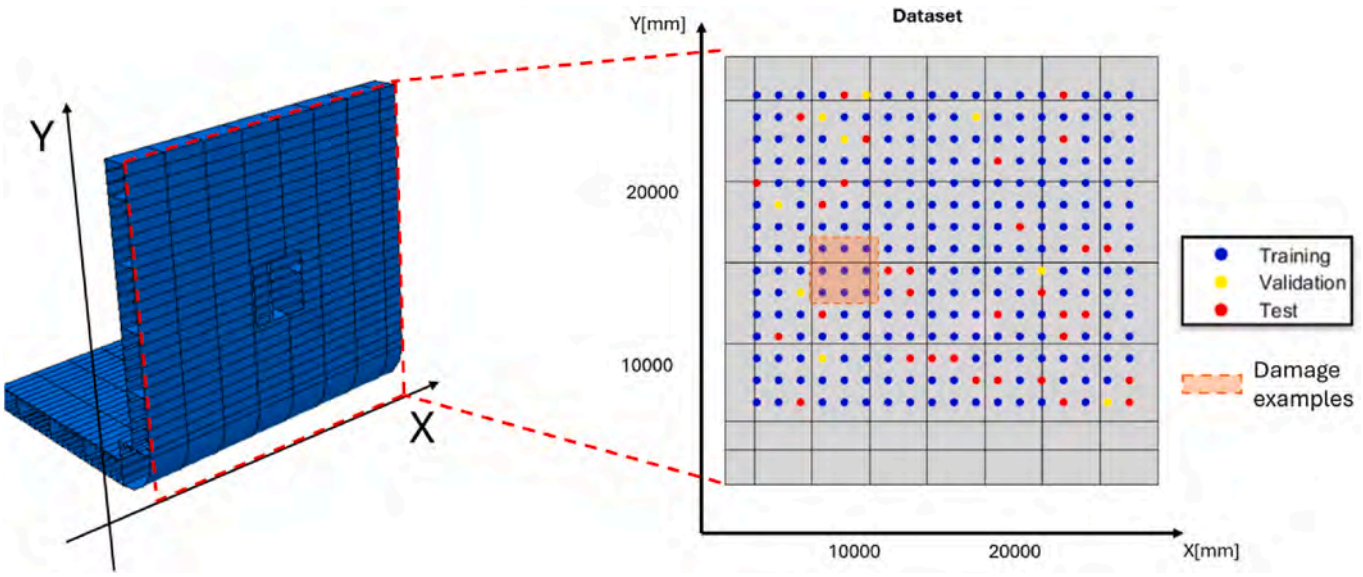

Fig. 15. Explanation of the subdivision of the dataset into training, validation and test sets.

The validation procedure with realistic damage geometries was carried out in several steps. First, a subset of representative damage locations was selected from the test set. The aim was to avoid reusing the entire dataset—which could bias the evaluation—and instead focus on a smaller number of cases capable of highlighting the generalization capability of the proposed method. For each selected location, high-fidelity dynamic explicit blast simulations were performed, generating complex damage patterns. The final geometries, extracted at the last simulation frame when the blast-induced deformation had stabilized, were then taken as reference for subsequent iFEM reconstructions.

On these blast-damaged geometries, the same sensor configuration defined in Paragraph 3.3 was applied, ensuring consistency with the training phase. In other words, both the input sensor network (feeding the iFEM) and the test sensor network (providing the anomaly index values) were positioned at the same locations as in the simplified models, even though the underlying geometry now included realistic damage. The iFEM procedure was executed in the same manner as before, reconstructing the strain and displacement fields under the assumption of a healthy structure. The resulting anomaly index values computed at the test sensors were then fed into the pre-trained DNNs, which provided predictions of the damage coordinates.

In this way, the proposed framework was evaluated not only on idealized cases but also on realistic, physically consistent damage scenarios. This step confirms the ability of the combined iFEM–anomaly index–DNNs strategy to handle the complexities of real blast-induced structural failures, thereby reinforcing its potential as a robust tool for structural health monitoring and damage localization in large-scale naval applications.

3.7. Damage identification and localization results

The performance of the two DNN models on previously unseen combinations of damage positions was carefully evaluated to assess their generalization capability. The results are summarized in Fig. 16 for the models described in Section 3.2. In particular, Fig. 16a reports the reconstruction error for all test cases, considering both the X and Y coordinates of the damage center. For each simulated damage position in the test set, the prediction error was computed as the Euclidean distance between the actual (X, Y) and the predicted $(\widehat{X}, \widehat{Y})$ damage coordinates, according to Equation (13).

$$\textit{Prediction Error} = \sqrt{(X - \widehat{X})^2 + (Y - \widehat{Y})^2} \tag{13}$$

This metric provides an intuitive measure of the localization accuracy, as it directly quantifies the spatial distance between real and reconstructed damage centers.

Fig. 16b and c presents a comparison between the predicted and actual coordinates separately for the two networks. Both plots confirm that the trained models are capable of correctly capturing the position of the damage, with predictions clustering closely around the reference diagonal line. The X-coordinate network shows slightly better agreement with the true values, while the Y-coordinate model tends to exhibit higher variance and larger deviations in some cases. This behavior is consistent with what was observed during training, where the Y network required a stronger regularization to ensure stable convergence.

Fig. 16d complements this analysis by showing the evolution of the loss function during training for the X-coordinate network. The curve highlights the progressive reduction of the mean squared error across epochs, ultimately stabilizing at a low value and confirming both the adequacy of the chosen hyperparameters and the absence of overfitting phenomena. This evidence supports the robustness of the training process and provides further confidence in the reliability of the model's predictions.

From a global perspective, the networks demonstrated accurate and robust performance across all test cases involving simplified damage scenarios. As expected, the prediction error increases when the damage is located farther from the sensor network, reflecting the reduced sensitivity of the anomaly index in regions that are weakly instrumented. Nevertheless, the maximum error observed in the test set—approximately 500 mm—remains acceptable when compared to the typical size of the imposed damage (5×5 m). This level of accuracy ensures that the proposed framework can identify the correct damage compartment or structural region, which is the critical information needed for decision-making in marine and offshore applications. In fact, unlike in aerospace or precision mechanical contexts, in naval practice it is not necessary to pinpoint the defect with millimetric accuracy. Rather, what matters most is to determine the affected compartment or zone of the hull to support timely safety measures and operational decisions.

Finally, the generalization capability of the models was further confirmed through the evaluation of representative test cases involving realistic blast-induced damages (see Section 3.1). As shown in Fig. 17, the DNNs were able to maintain satisfactory predictive accuracy even in the presence of geometrically complex and physically consistent damage configurations. This result demonstrates that training the networks on a database of simplified but systematically generated damage scenarios

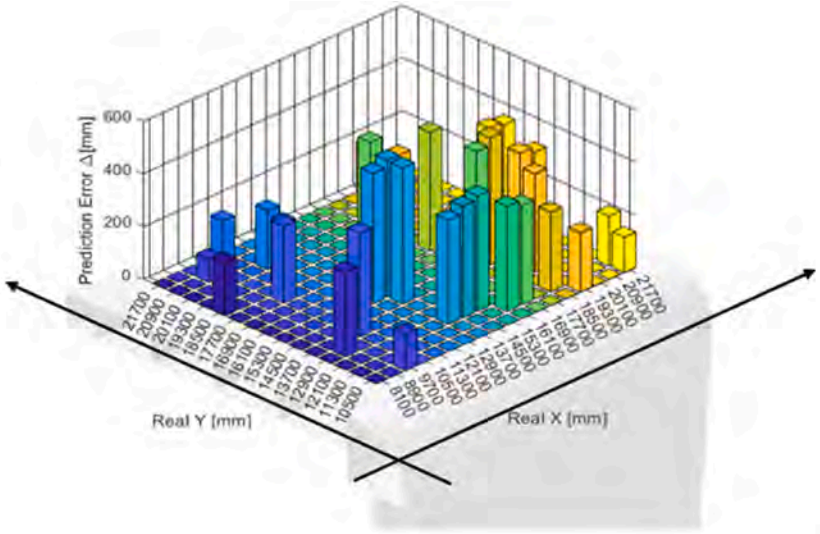

(a)

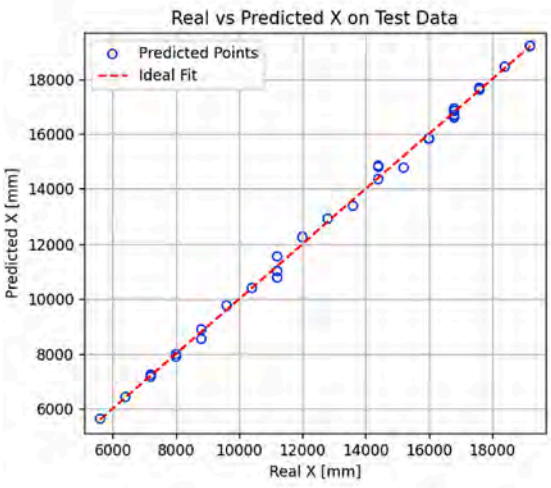

(b)

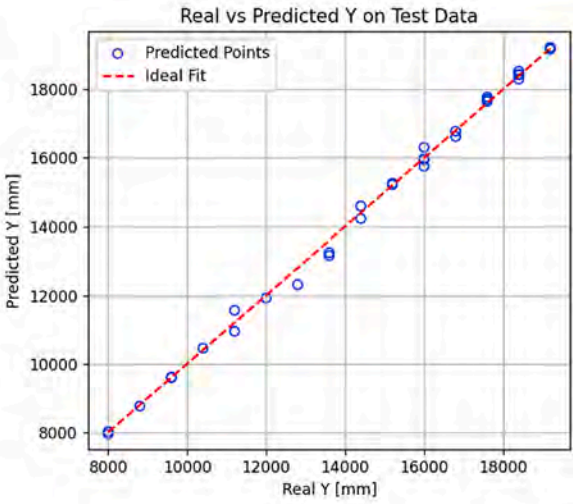

(c)

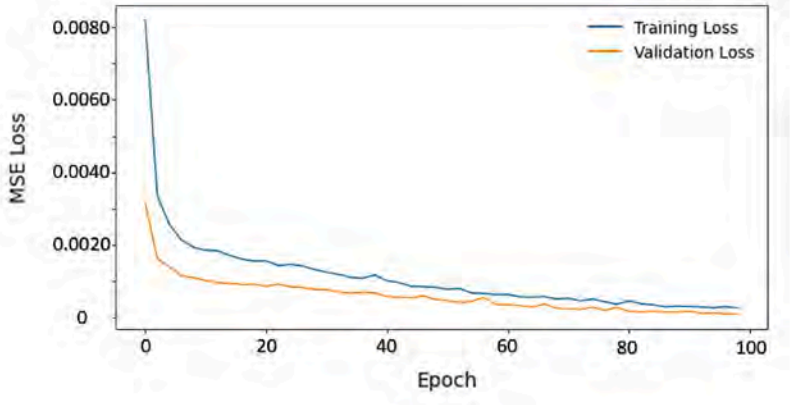

(d)

Fig. 16. Predictions of the DNNs: (a) column chart representing the Prediction Error of all test cases considered, (b) comparison prediction vs real *X* coordinate, (c) comparison prediction vs real *Y* coordinate and (d) example of the loss function history related to the DNN that predicts *X* coordinate.

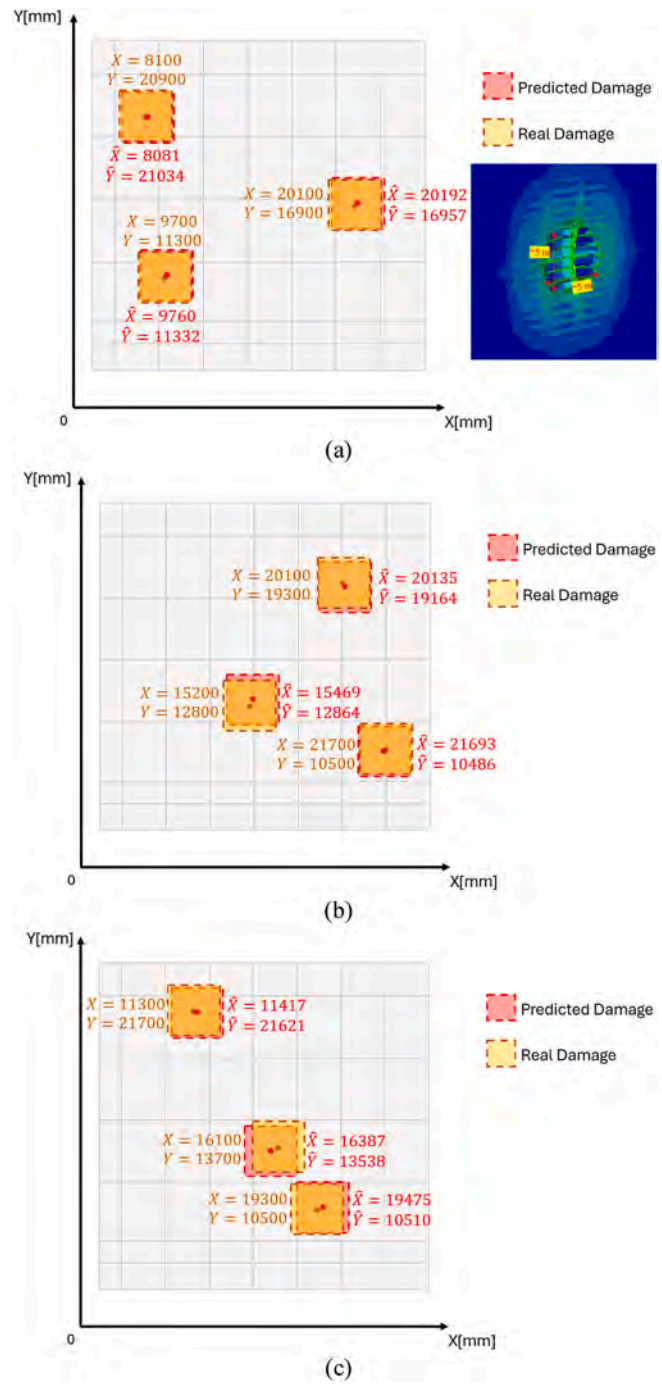

Fig. 17. Visual representation of the real damage (not simulated) and the reconstructed one for some representative test case scenarios.

provides a sufficiently rich basis for extending the methodology to more realistic situations. Taken together, these findings confirm that the integration of iFEM, anomaly index, and DNNs can deliver a robust and scalable tool for structural health monitoring and damage localization in large-scale naval structures subjected to extreme loading conditions.

Finally, a computation time assessment was carried out to verify the real-time feasibility of the proposed framework. All computations for on-line operation (iFEM reconstruction + anomaly index + DNN inference) were benchmarked on the same workstation used throughout the study (Intel® Core™ i9-14900K 3.20 GHz, 128 GB RAM, CPU-only). Training and high-fidelity/simplified simulations are performed offline and are not part of real-time use.

- iFEM reconstruction per update: ≈0.48 s.
- Anomaly index computation at the four test sensors: ≈0.002 s.
- DNN inference (two regressors for X and Y): ≈0.05 s.
- Total end-to-end latency per update (iFEM → Anomaly index → DNNs): ≈0.53 s.

4. Conclusions

This study has introduced a robust framework for the real-time identification of damage locations in ships subjected to extreme environmental conditions. The approach integrates the inverse Finite Element Method (iFEM), the anomaly index formulation, and Machine Learning techniques, representing the first marine engineering application of this combined methodology. Within the framework, iFEM enables the rapid reconstruction of the full displacement field from discrete strain measurements, while the anomaly index provides a load-independent tool for detecting and localizing damage.

Applying iFEM and the anomaly index to large and complex ship structures poses challenges, primarily due to the extensive number of sensors typically required for effective Structural Health Monitoring (SHM). To overcome this limitation, two DNNs were developed to learn the relationship between a minimal set of anomaly index values—obtained from just four rosette-based sensors—and the precise coordinates of air-blast-induced damage. The framework was demonstrated on a representative portion of the MOL Confort containership, with a dataset of approximately 270 simulated cases generated according to classification society rules.

Although the present work focused on blast-induced damage as a representative extreme event, the proposed framework is not limited to this loading condition. Thanks to the load-independent nature of the iFEM-based Anomaly Index and the flexibility of the machine learning models, the methodology can be readily extended to other critical scenarios such as collision, grounding, extreme wave impacts, or progressive degradation processes like corrosion and fatigue. In these cases, only the training dataset needs to be adapted to the specific damage typology, while the overall structure of the framework remains unchanged. This highlights the general applicability of the approach as a versatile SHM strategy for naval and offshore structures beyond blast events.

The methodology followed a two-step strategy: high-fidelity simulations were first employed to assess the extent of damage in an extreme blast scenario, and these results were subsequently simplified to generate a large dataset for training and validation of the DNNs. The trained models were then tested against high-fidelity blast-induced damage cases, thereby verifying their ability to generalize to more realistic conditions.

Sensor placement was carefully designed to reflect practical constraints in marine environments, with strain sensors located exclusively on the interior of the ship's structure to avoid issues related to seawater exposure. Despite this minimal configuration, the proposed DNNs achieved accurate localization of damage, with prediction errors remaining within acceptable limits. As expected, errors increased with damage distance from the sensor network; nevertheless, the performance was sufficient to identify the affected compartment, which is the critical requirement for naval applications. Remarkably, the use of only four rosette-based sensors proved effective in monitoring the compartment, demonstrating the cost-effectiveness and practical viability of the proposed SHM strategy.

Overall, the integration of iFEM, the anomaly index, and DNNs offers a fast, scalable, and computationally efficient framework for structural health monitoring of ships under extreme loading conditions. The proposed methodology enhances crew safety, supports timely maintenance and repair decisions, and strengthens resilience against future threats, thereby providing significant potential for real-world implementation in marine and offshore structures.

It is acknowledged that the validation presented in this work is

entirely simulation-based, as no experimental or field data are currently available. This limitation arises from the intrinsic challenges of performing full-scale experimental tests on naval or offshore structures subjected to blast loads, due to safety, cost, and confidentiality constraints. Nevertheless, the numerical framework employed—based on the CONWEP model derived from the Kingery–Bulmash experimental database—ensures that the blast loading is physically grounded in experimental evidence. Furthermore, the capability of the proposed framework to generalize from simplified to high-fidelity damage scenarios demonstrates its robustness. Future work will focus on extending the validation to experimental datasets, thereby accounting for sensor noise, environmental variability, and installation tolerances.

CRediT authorship contribution statement

Jacopo Bardiani: Writing – review & editing, Writing – original draft, Validation, Methodology, Investigation, Formal analysis, Data curation, Conceptualization. **Roberto Faure Ragani:** Writing – review & editing, Writing – original draft, Visualization, Validation, Methodology, Investigation, Formal analysis, Data curation, Conceptualization. **Andrea Manes:** Writing – review & editing, Supervision, Resources, Project administration, Methodology. **Claudio Sbarufatti:** Writing – review & editing, Supervision, Resources, Project administration, Methodology, Conceptualization. **Adnan Kefal:** Writing – review & editing, Methodology, Conceptualization.

Data availability statement

The data given in this article are the data supporting the results of this study are available upon request.

Declaration of competing interest

The authors declare that they have no known competing financial interests or personal relationships that could have appeared to influence the work reported in this paper.

Acknowledgements

The author(s) disclosed receipt of the following financial support for the research, authorship, and/or publication of this article.

References

Abdollahzadeh, M.A., Kefal, A., Yildiz, M., 2020. A comparative and review study on shape and stress sensing of flat/curved shell geometries using C0-continuous family of iFEM elements. Sensors 20 (14), 3808. https://doi.org/10.3390/s20143808.

Aravanis, G.I., Silionis, N.E., Anyfantis, K.N., 2023. Damage detection in ship hull structures under operational variability through strain sensing. Ocean Eng. 286. https://doi.org/10.1016/j.oceaneng.2023.115537.

Bardiani, J., Manes, A., Giglio, M., Sbarufatti, C., 2024. Shape sensing and damage identification with iFEM on a double bottom structure of a containership. In: Concli, F., Maccioni, L., Vidoni, R., Matt, D.T. (Eds.), Latest Advancements in Mechanical Engineering. ISIEA 2024. Lecture Notes in Networks and Systems, 1124. Springer, Cham. https://doi.org/10.1007/978-3-031-70462-8_22.

Bardiani, J., Oppezzo, C., Manes, A., Sbarufatti, C., 2025a. An inverse FEM for structural health monitoring of a containership: sensor network optimization for accurate displacement, strain, and internal force reconstruction. Sensors 25 (1), 276. https://doi.org/10.3390/s25010276.

Bardiani, J., Lomazzi, L., Manes, A., Sbarufatti, C., 2025b. A machine learning-based tool to correlate coupled and uncoupled numerical simulations for submerged plates subjected to non-contact underwater explosions. J. Mar. Sci. Appl. 1–20. https://doi.org/10.1007/s11804-025-00624-5.

Bardiani, J., Mazzolatti, C., Manes, A., Sbarufatti, C., 2025c. A hybrid approach to enhance decision-making in marine structures: combining sensor data with human perception. Results Eng. 27, 105670. https://doi.org/10.1016/j.rineng.2025.105670.

Belur, M.Y., Bilgin, M.H., Fassois, S.D., Kefal, A., 2025. Inverse finite element methodology for high-resolution mode shape reconstruction of plates and shells under random excitation. Comput. Struct. 311, 107721. https://doi.org/10.1016/j.compstruc.2025.107721.

Bursuc, A., Munteanu, C., Rus, S., 2024. Overview on sea drones evolution and their use in modern warfare. Land Forces Academy Review 29, 195–209. https://doi.org/10.2478/raft-2024-0021.

Cerracchio, P., Gherlone, M., Di Sciuva, M., Tessler, A., 2015. A novel approach for displacement and stress monitoring of sandwich structures based on the inverse finite element method. Compos. Struct. 127, 69–76. https://doi.org/10.1016/j.compstruct.2015.02.081.

Colombo, L., Sbarufatti, C., Giglio, M., 2019. Definition of a load adaptive baseline by inverse finite element method for structural damage identification. Mech. Syst. Signal Process. 120, 584–607. https://doi.org/10.1016/j.ymssp.2018.10.041.

Colombo, L., Oboe, D., Sbarufatti, C., Cadini, F., Russo, S., Giglio, M., 2021. Shape sensing and damage identification with iFEM on a composite structure subjected to impact damage and non-trivial boundary conditions. Mech. Syst. Signal Process. 148, 107163. https://doi.org/10.1016/j.ymssp.2020.107163.

Deraemaeker, A., Reynders, E., De Roeck, G., Kullaa, J., 2008. Vibration-based structural health monitoring using output-only measurements under changing environment. Mech. Syst. Signal Process. 22, 34–56. https://doi.org/10.1016/j.ymssp.2007.07.004.

Draganić, H., Sigmund, V., 2012. Blast loading on structures. Teh. Vjesn. 19 (3), 643–652. https://hrcak.srce.hr/86741.

Ehlers, S., Broekhuijsen, J., Alsos, H.S., Biehl, F., Tabri, K., 2008. Simulating the collision response of ship side structures: a failure criteria benchmark study. Int. Shipbuild. Prog. 55, 127–144. https://doi.org/10.3233/ISP-2008-0042.

Esposito, M., 2024. A novel shape sensing approach based on the coupling of modal virtual sensor expansion and iFEM: numerical and experimental assessment on composite stiffened structures. Comput. Struct. 305. https://doi.org/10.1016/j.compstruc.2024.107520.

Esposito, M., Roy, R., Surace, C., Gherlone, M., 2023. Hybrid shell-beam inverse finite element method for the shape sensing of stiffened thin-walled structures: formulation and experimental validation on a composite wing-shaped panel. Sensors 23 (13), 5962. https://doi.org/10.3390/s23135962.

Gardner, P.A., 2018. On Novel Approaches to Model-based Structural Health Monitoring in the Faculty of Engineering.

Ghasemzadeh, M., Mokhtari, M., Bilgin, M.H., Kefal, A., 2023. Pitting corrosion identification approach based on inverse finite element method for marine structure applications. Ocean Eng. 273, 113953. https://doi.org/10.1016/j.oceaneng.2023.113953.

Gherlone, M., Cerracchio, P., Mattone, M., Di Sciuva, M., Tessler, A., 2012. Shape sensing of 3D frame structures using an inverse finite element method. Int. J. Solid Struct. 49 (22), 3100–3112. https://doi.org/10.1016/j.ijsolstr.2012.06.009.

Gherlone, M., Cerracchio, P., Mattone, M., Di Sciuva, M., Tessler, A., 2014. An inverse finite element method for beam shape sensing: theoretical framework and experimental validation. Smart Mater. Struct. 23 (4), 045027. https://doi.org/10.1088/0964-1726/23/4/045027.

Guo, K., Yang, Z., Yu, C.H., Buehler, M.J., 2021. Artificial intelligence and machine learning in design of mechanical materials. Mater. Horiz. 8 (4), 1153–1172. https://doi.org/10.1039/D0MH01451F.

Hinton, G.E., Simon, O., Yee-Whye, T., 2006. A fast learning algorithm for deep belief nets. Neural Comput. 18 (7), 1527–1554.

Iacs, 2024. Common Structural Rules for Bulk Carriers and Oil Tankers.

Johnson, G.R., 1983. A constitutive model and data for metals subjected to large strains, high strain rates and high temperatures. Proc. 7th Int. Symp. Ballistics, The Hague, Netherlands.

Kefal, A., 2019. An efficient curved inverse-shell element for shape sensing and structural health monitoring of cylindrical marine structures. Ocean Eng. 188, 106262. https://doi.org/10.1016/j.oceaneng.2019.106262.

Kefal, A., Oterkus, E., 2016. Displacement and stress monitoring of a panamax containership using inverse finite element method. Ocean Eng. 119, 16–29. https://doi.org/10.1016/j.oceaneng.2016.04.025.

Kefal, A., Oterkus, E., 2020. Isogeometric iFEM analysis of thin shell structures. Sensors 20 (9), 2685. https://doi.org/10.3390/s20092685.

Kefal, A., Oterkus, E., Tessler, A., Spangler, J.L., 2016. A quadrilateral inverse-shell element with drilling degrees of freedom for shape sensing and structural health monitoring. Eng. Sci. Technol. Int. J. 19, 1299–1313. https://doi.org/10.1016/j.jestch.2016.03.006.

Kefal, A., Tessler, A., Oterkus, E., 2017. An enhanced inverse finite element method for displacement and stress monitoring of multilayered composite and sandwich structures. Compos. Struct. 179, 514–540. https://doi.org/10.1016/j.compstruct.2017.07.078.

Kefal, A., Mayang, J.B., Oterkus, E., Yildiz, M., 2018. Three dimensional shape and stress monitoring of bulk carriers based on iFEM methodology. Ocean Eng. 147, 256–267. https://doi.org/10.1016/j.oceaneng.2017.10.040.

Kefal, A., Tabrizi, I.E., Tansan, M., Kisa, E., Yildiz, M., 2021a. An experimental implementation of inverse finite element method for real-time shape and strain sensing of composite and sandwich structures. Compos. Struct. 258, 113431. https://doi.org/10.1016/j.compstruct.2020.113431.

Kefal, A., Tabrizi, I.E., Yildiz, M., Tessler, A., 2021b. A smoothed iFEM approach for efficient shape-sensing applications: numerical and experimental validation on composite structures. Mech. Syst. Signal Process. 152, 107486. https://doi.org/10.1016/j.ymssp.2020.107486.

Kefal, A., Diyaroglu, C., Yildiz, M., Oterkus, E., 2022. Coupling of peridynamics and inverse finite element method for shape sensing and crack propagation monitoring of plate structures. Comput. Methods Appl. Mech. Eng. 391, 114520. https://doi.org/10.1016/j.cma.2021.114520.

Kefal, A., Bilgin, M.H., Kendibilir, A., 2024. Particle inverse method for full-field displacement and crack propagation monitoring from discrete sensor measurements.

Comput. Methods Appl. Mech. Eng. 432, 117369. https://doi.org/10.1016/j.cma.2024.117369.
Kingery, C.N., Bulmash, G., 1984. Airblast parameters from TNT spherical air burst and hemispherical surface burst. US Army Armament and Development Center, Ballistic Research Laboratory.
Kroworz, A., Katunin, A., 2018. Non-destructive testing of structures using optical and other methods: a review. SDHM Structural Durability and Health Monitoring 12, 1–17. https://doi.org/10.3970/sdhm.2018.012.001.
Li, M., Kefal, A., Cerik, B.C., Oterkus, E., 2020. Dent damage identification in stiffened cylindrical structures using inverse finite element method. Ocean Eng. 198. https://doi.org/10.1016/j.oceaneng.2020.106944.
Li, M., Wu, Z., Jia, D., Qiu, S., He, W., 2022. Structural damage identification using strain mode differences by the iFEM based on the convolutional neural network (CNN). Mech. Syst. Signal Process. 165. https://doi.org/10.1016/j.ymssp.2021.108289.
Lin, L., Zhi, X.-D., Fan, F., Meng, S.-J., Su, J.-J., 2014. Determination of parameters of Johnson-Cook models of Q235B steel. J. Vib. Shock 33, 153–158+172. https://doi.org/10.13465/j.cnki.jvs.2014.09.028.
Lloyd's Register, 2019. Rules and Regulations for the Classification of Naval Ships.
Oboe, D., Colombo, L., Sbarufatti, C., Giglio, M., 2021a. Shape sensing of a complex aeronautical structure with inverse finite element method. Sensors 21 (4), 1388. https://doi.org/10.3390/s21041388.
Oboe, D., Colombo, L., Sbarufatti, C., Giglio, M., 2021b. Comparison of strain pre-extrapolation techniques for shape and strain sensing by iFEM of a composite plate subjected to compression buckling. Compos. Struct. 262, 113587. https://doi.org/10.1016/j.compstruct.2021.113587.
Oboe, D., Sbarufatti, C., Giglio, M., 2022. Physics-based strain pre-extrapolation technique for inverse finite element method. Mech. Syst. Signal Process. 177. https://doi.org/10.1016/j.ymssp.2022.109167.
Oboe, D., Poloni, D., Sbarufatti, C., Giglio, M., 2023. Towards automatic crack size estimation with iFEM for structural health monitoring. Sensors 23. https://doi.org/10.3390/s23073406.
Papa, U., Russo, S., Lamboglia, A., Del Core, G., Iannuzzo, G., 2017. Health structure monitoring for the design of an innovative UAS fixed wing through inverse finite element method (iFEM). Aero. Sci. Technol. 69, 439–448. https://doi.org/10.1016/j.ast.2017.07.005.
Pettyjohn, S., Dennis, H., Campbell, M., 2024. Swarms over the strait: drone warfare in a future fight to defend Taiwan. Center for a New American Security.
Poloni, D., Oboe, D., Sbarufatti, C., Giglio, M., 2023a. Towards a stochastic inverse finite element method: a Gaussian process strain extrapolation. Mech. Syst. Signal Process. 189. https://doi.org/10.1016/j.ymssp.2022.110056.
Poloni, D., Oboe, D., Sbarufatti, C., Giglio, M., 2023b. Variable thickness strain pre-extrapolation for the inverse finite element method. Sensors 23. https://doi.org/10.3390/s23031733.
Prabowo, A.R., Ridwan, R., Tuswan, T., Sohn, J.M., Surojo, E., Imaduddin, F., 2022. Effect of the selected parameters in idealizing material failures under tensile loads: benchmarks for damage analysis on thin-walled structures. Curved Layer. Struct. 9, 258–285. https://doi.org/10.1515/cls-2022-0021.
Rice, J.R., Tracey, D.M., 1969. On the ductile enlargement of voids in triaxial stress fields. J. Mech. Phys. Solid. 17, 201–217. https://doi.org/10.1016/0022-5096(69)90033-7.
Roy, R., Gherlone, M., 2023. Delamination and skin-spar debond detection in composite structures using the inverse finite element method. Materials 16. https://doi.org/10.3390/ma16051969.
Roy, R., Tessler, A., Surace, C., Gherlone, M., 2020. Shape sensing of plate structures using the inverse finite element method: investigation of efficient strain–sensor patterns. Sensors 20 (24), 7049. https://doi.org/10.3390/s20247049.
Roy, R., Gherlone, M., Surace, C., Tessler, A., 2021. Full-field strain reconstruction using uniaxial strain measurements: application to damage detection. Appl. Sci. 11, 1–22. https://doi.org/10.3390/app11041681.
Roy, R., Tessler, A., Surace, C., Gherlone, M., 2022. Efficient shape sensing of plate structures using the inverse finite element method aided by strain pre-extrapolation. Thin-Walled Struct. 180. https://doi.org/10.1016/j.tws.2022.109798.
Rytter, A., Brincker, R., Hansen, L.P., 1993. Vibration Based Inspection of Civil Engineering Structures.
Salazar-Domínguez, C.M., Hernández-Hernández, J., Rosas-Huerta, E.D., Iturbe-Rosas, G.E., Herrera-May, A.L., 2021. Article structural analysis of a barge midship section considering the still water and wave load effects. J. Mar. Sci. Eng. 9, 1–21. https://doi.org/10.3390/jmse9010099.
Sbarufatti, C., Manes, A., Giglio, M., 2013. Performance optimization of a diagnostic system based upon a simulated strain field for fatigue damage characterization. Mech. Syst. Signal Process. 40, 667–690. https://doi.org/10.1016/j.ymssp.2013.06.003.
Sbarufatti, C., Manson, G., Worden, K., 2014. A numerically-enhanced machine learning approach to damage diagnosis using a lamb wave sensing network. J. Sound Vib. 333, 4499–4525. https://doi.org/10.1016/j.jsv.2014.04.059.
Silling, S.A., Weckner, O., Askari, E., Bobaru, F., 2010. Crack nucleation in a peridynamic solid. Int. J. Fract. 162, 219–227.
Silva-Campillo, A., Pérez-Arribas, F., Suárez-Bermejo, J.C., 2023. Health-monitoring systems for marine structures: a review. Sensors. https://doi.org/10.3390/s23042099.
Simonsen, B.C., Törnqvist, R., 2004. Experimental and numerical modelling of ductile crack propagation in large-scale shell structures. Mar. Struct. 17, 1–27. https://doi.org/10.1016/j.marstruc.2004.03.004.
Smith, M., 2009. ABAQUS/standard User's Manual, Version 6.9. Dassault Systèmes Simulia Corp, United States.
Song, X., Liang, D., 2018. Dynamic displacement prediction of beam structures using fiber bragg grating sensors. Optik 158, 1410–1416. https://doi.org/10.1016/j.ijleo.2018.01.013.
Tessler, A., Spangler, J.L., 2003. A Variational Principle for Reconstruction of Elastic Deformations in Shear Deformable Plates and Shells.
Tessler, A., Spangler, J.L., 2005. A least-squares variational method for full-field reconstruction of elastic deformations in shear-deformable plates and shells. Comput. Methods Appl. Mech. Eng. 194, 327–339. https://doi.org/10.1016/j.cma.2004.03.015.
Tessler, A., Spangler, J.L., 2024. Inverse FEM for full-field reconstruction of elastic deformations in shear deformable plates and shells. In: Proceedings of 2nd European Workshop on Structural Health Monitoring. Munich, Germany.
Tessler, A., Di Sciuva, M., Gherlone, M., 2010. A consistent refinement of first-order shear deformation theory for laminated composite and sandwich plates using improved zigzag kinematics. J. Mech. Mater. Struct. 5 (2), 341–367.
Zhao, F., Bao, H., Liu, J., Li, K., 2021. Shape sensing of multilayered composite and sandwich beams based on refined Zigzag theory and inverse finite element method. Compos. Struct. 261, 113321. https://doi.org/10.1016/j.compstruct.2020.113321.
Zhou, Z.H., 2021. Machine Learning, Machine Learning. Springer Nature. https://doi.org/10.1007/978-981-15-1967-3.
Zhu, H., Du, Z., Tang, Y., 2022a. Numerical study on the displacement reconstruction of subsea pipelines using the improved inverse finite element method. Ocean Eng. 248, 110763. https://doi.org/10.1016/j.oceaneng.2022.110763.
Zhu, H., Du, Z., Tang, Y., 2022b. Automatic free span assessment for subsea pipelines using static strain data. Ocean Eng. 263, 112413. https://doi.org/10.1016/j.oceaneng.2022.112413.